Non-Oberbeck-Boussinesq effects in turbulent thermal convection in ethane close to the critical point

Guenter Ahlers,[1] Enrico Calzavarini,[2] Francisco Fontenele Araujo,[2] Denis Funfschilling,[3] Siegfried Grossmann,[4] Detlef Lohse,[2] and Kazuyasu Sugiyama[2]

[1]*Department of Physics and iQCD, University of California, Santa Barbara, CA 93106*
[2]*Department of Applied Physics and J. M. Burgers Centre for Fluid Dynamics,*
University of Twente, 7500 AE Enschede, The Netherlands
[3]*LSGC CNRS - GROUPE ENSIC, BP 451, 54001 Nancy Cedex, France*
[4]*Department of Physics, Philipps-University of Marburg, Renthof 6, D-35032 Marburg, Germany*
(Dated: February 22, 2008)

As shown in earlier work (Ahlers *et al.*, J. Fluid Mech. **569**, 409 (2006)), non-Oberbeck Boussinesq (NOB) corrections to the center temperature in turbulent Rayleigh-Bénard convection *in water* and also *in glycerol* are governed by the temperature dependences of the kinematic viscosity and the thermal diffusion coefficient. If the working fluid is *ethane close to the critical point* the origin of non-Oberbeck-Boussinesq corrections is very different, as will be shown in the present paper. Namely, the main origin of NOB corrections then lies in the strong temperature dependence of the isobaric thermal expansion coefficient $\beta(T)$. More precisely, it is the nonlinear T-dependence of the density $\rho(T)$ in the buoyancy force which causes another type of NOB effect. We demonstrate that through a combination of experimental, numerical, and theoretical work, the latter in the framework of the extended Prandtl-Blasius boundary layer theory developed by Ahlers *et al.*, J. Fluid Mech. **569**, 409 (2006). The latter comes to its limits, if the temperature dependence of the thermal expension coefficient $\beta(T)$ is significant. The new measurements reported here cover the ranges $2.1 \lesssim Pr \lesssim 3.9$ and $5 \times 10^9 \lesssim Ra \lesssim 2 \times 10^{12}$ and are for cylindrical samples of aspect ratios 1.0 and 0.5.

I. INTRODUCTION

Fluid motion in the presence of temperature gradients is an important phenomenon in nature and industrial processes. Among the many examples are oceanic streams, cloud motions, and gusts of wind that can be felt on a human scale. The paradigmatical system for such thermally driven flows is the Rayleigh-Bénard (RB) setup: a fluid-filled container heated from below and cooled from above. In this classical problem, the flow is determined by the scale and geometry of the container, the material properties of the working fluid, and the top-down temperature difference $\Delta \equiv T_b - T_t > 0$. In the last two decades, considerable progress has been achieved in our understanding of global and local properties and the flow organization of turbulent RB convection, through a combination of experimental (see e.g. [1, 2, 3, 4, 5, 6, 7, 8, 9, 10, 11, 12, 13, 14, 15, 16, 17, 18, 19, 20, 21, 22, 23, 24]), numerical (see e.g. [25, 26, 27, 28, 29, 30, 31, 32, 33, 34, 35]), and theoretical work (see e.g. [36, 37, 38]).

The temperature difference in a RB cell can be increased in a controlled way. However, in principle the transport coefficients of the fluid can depend on the local temperature and density and thus vary across the height L of the container. Since space-dependent properties of such kind are undesirable in first instance, one tends to restrict the convection regime to sufficiently small intervals of Δ. But even so, further simplifications are progressively required in the analysis of RB convection. In this spirit, a standard approximation due to Oberbeck [39] and Boussinesq [40] assumes that (see also [41, 42]):

OB.1 The dynamic viscosity η, the thermal conductivity Λ, the thermal expansivity β, and the isobaric specific heat c_P are constant throughout the fluid.

OB.2 Density variations are taken into account only in the buoyancy force term.

OB.3 The temperature dependence of the density ρ is linearized in the buoyancy force as:

$$\rho(T) = \rho_m - \rho_m \beta_m (T - T_m), \tag{1}$$

where $T_m \equiv (T_b + T_t)/2$ is the arithmetic mean temperature between the plates and $X_m = X(T_m)$ denotes the fluid property X evaluated at T_m.

Next to the aspect ratio, within the OB approximation two dimensionless parameters characterize the RB flow: The Prandtl number $Pr \equiv \nu_m/\kappa_m$ follows from the ratio between the kinematic viscosity $\nu_m \equiv \eta_m/\rho_m$ and the thermal diffusivity $\kappa_m \equiv \Lambda_m/(\rho_m c_{P,m})$. The dimensionless thermal driving can be conveniently represented by the Rayleigh number $Ra \equiv \beta_m g L^3 \Delta/(\nu_m \kappa_m)$, where g denotes the gravitational acceleration.

The manner in which high Rayleigh numbers are achieved is crucial for the emergence of non-Oberbeck-Boussinesq effects (NOB). Since turbulent convection may involve spatiotemporal changes in the fluid properties, considerable efforts have been devoted to the identification of dominating sources of NOB effects. In liquids like water [43] and glycerol [44], [45], for example, NOB effects are dominated by deviations from (OB.1) since the viscosity strongly decreases with temperature. On the other hand, when the working fluid is gaseous ethane

[46], deviations from (OB.1) and (OB.2) lead to NOB effects stronger than those in the aforementioned liquids.

In the present study, we shall focus on deviations from (OB.3) by considering the nonlinear temperature dependence of the buoyancy force. In particular, ethane close to its critical point [47] is chosen as the working fluid and the temperature T_c in the center of the container is measured as indicator of NOB effects.

There are two possibilities to characterize the physics beyond condition OB.3 as described by eq. (1), if the density $\rho(T)$ has a strong nonlinear T-dependence. First, one can introduce a T-dependent thermal expansion function $\hat{\beta}(T)$ instead of β_m, defined in terms of the density $\rho(T)$ by

$$\rho(T) \equiv \rho_m - \rho_m(T - T_m)\hat{\beta}(T). \tag{2}$$

Second, one refers to the common isobaric thermal expansion coefficient $\beta(T)$, defined as usual by

$$\beta(T) \equiv -\frac{1}{\rho(T)}\frac{\partial \rho(T)}{\partial T}|_P, \tag{3}$$

which now is temperature dependent. Both are related by $\beta(T) = -\partial \log[1 - (T - T_m)\hat{\beta}(T)] / \partial T$. Under the condition OB.3 of linear T-dependence of ρ the thermal expansion function is constant, $\hat{\beta} = \beta_m$, while the expansion coefficient $\beta(T)$ is given by $\beta(T) = \beta_m/[1 - (T - T_m)\beta_m]$, still depending on temperature. Of course all three coincide at T_m. An advantage of considering the thermal expansion coefficient $\beta(T)$ is that it is a well defined thermodynamic derivative. The advantage of $\hat{\beta}(T)$ on the other hand is that it immediately reflects the nonlinear T-dependence of $\rho(T)$. Also $\beta(T)$ refers to a single thermodynamic state and describes the local T-slope on an isobar (normalized by the local density), while $\hat{\beta}(T)$ refers to a pair of states, namely to the reference state T_m in addition to T and describes the secant to the $\rho(T)$-curve (normalized by the reference density). $\hat{\beta}(T)$ will therefore in general vary less with T than $\beta(T)$.

It will turn out that it is the significantly different T-dependence of $\hat{\beta}(T)$ (or $\beta(T)$) on the two sides of the critical isochore of ethane, which leads to opposite shifts of the center (bulk) temperature T_c, yielding $T_c < T_m$ on the gas-like (i.e. high-temperature, see Fig. 1 below) side and $T_c > T_m$ on the liquid-like (low-temperature) side. On the gas-like side $\hat{\beta}(T)$ increases from bottom to top and on the liquid-like side it decreases.

Our approach consists of three stages: boundary layer (BL) theory, experiments, and direct numerical simulations (DNS). First, we address in section II an extension of boundary layer theory that considers deviations from (OB.1) and (OB.2). Even though the buoyancy force is *not* included in the BL equations (only the *longitudinal* momentum is taken into account here), we compute $T_c(\Delta)$ for several pressures P_m. Then, experimental measurements of $T_c(\Delta)$ are presented in section III B and compared with BL results in section IV. Given the

significant discrepancies between part of them, we address in section V direct numerical simulations that explicitly consider deviations from (OB.3). In particular, for $T_m = 27°$ C and $P_m = 51.72$ bar, it is shown that NOB effects in ethane are dominated by the nonlinear dependence of the buoyancy force on temperature. Finally, our conclusions are summarized in section VI. Appendices A and B are devoted to the derivation of the boundary layer equations with variable transport coefficients and Appendix C compiles the Nusselt number corrections for the real and various hypothetical ethane-like fluids in a table.

II. BOUNDARY-LAYER THEORY

A central aspect in Rayleigh-Bénard convection is the understanding of the boundary layers formed along the bottom and top plates. Though they preserve a laminar character for $Ra \leq 10^{12}$, their instabilities impact the Nusselt number Nu (the effective heat flux relative to thermal conduction $\Lambda_m\Delta/L$) [48, 49]. As reported in references [43, 44, 46], BL flows of this nature are significantly influenced by the coupling between the fluid properties and the temperature gradient across the container. In particular, it was shown that NOB effects on T_c can be reasonably described by extending the Prandtl-Blasius boundary layer theory [50, 51]. Next we review such an extension and further assess its intrinsic limitations.

Assume that the density ρ, the temperature T, and the velocity $\mathbf{u}$ are stationary fields, which depend only on the longitudinal x and transverse z coordinates. Then, under the boundary-layer approximation, we write the continuity and the x-momentum equations as (see also appendix A 1):

$$\frac{\partial}{\partial x}\{\rho u_x\} + \frac{\partial}{\partial z}\{\rho u_z\} = 0, \tag{4}$$

$$\rho\left\{u_x\frac{\partial u_x}{\partial x} + u_z\frac{\partial u_x}{\partial z}\right\} = \frac{\partial}{\partial z}\left\{\eta\frac{\partial u_x}{\partial z}\right\}. \tag{5}$$

Here z measures the vertical distance from the bottom or top plates, respectively, the velocity components at $z = 0$ are subject to no-slip boundary conditions: $u_x(x,0) = 0$ and $u_z(x,0) = 0$. Moreover, in the bulk of the flow, u_x is supposed to match the large scale wind velocity U_c in the center (bulk) of the RB sample [52], i.e., $u_x(x,\infty) = U_c$. Note that within the BL theory we cannot calculate U_c; here we only have to assume that it is the same close to the top and the bottom BL which is supported by our numerical simulations reported in section V.

In the same spirit, the temperature field $T(x,z)$ is governed by (cf. appendix A 2):

$$\frac{\gamma}{\rho c_P}\frac{\partial}{\partial z}\left\{\Lambda\frac{\partial T}{\partial z}\right\} = u_x\frac{\partial T}{\partial x} + u_z\frac{\partial T}{\partial z} + \frac{\gamma - 1}{\beta}\left\{\frac{\partial u_x}{\partial x} + \frac{\partial u_z}{\partial z}\right\}, \tag{6}$$

where $\gamma \equiv c_P/c_V$ is the ratio between the isobaric and isochoric specific heats and $\beta = -\rho^{-1}\partial\rho/\partial T$ denotes the isobaric thermal expansion coefficient. At the plates $T(x,0) = T_{b,t}$ and in the bulk (center) of the flow $T(x,\infty) = T_c$.

The coupling between the bottom and top boundary layers is determined (cf. [43]) by the heat fluxes $Q_{b,t}$ through the plates, considered to be equal:

$$Q_b = -\Lambda_b \left.\frac{\partial T}{\partial z}\right|_b = -\Lambda_t \left.\frac{\partial T}{\partial z}\right|_t = Q_t. \quad (7)$$

This condition establishes an implicit dependence of the center temperature T_c on the heat fluxes $Q_b = Q_t = Q$. Note again that both the dynamic viscosity η and the heat conductivity Λ depend on both temperature and density, i.e., $\eta(T,\rho)$ and $\Lambda(T,\rho)$. Before addressing the technicalities around the (numerical) integration of equations (4)–(7), we shall benefit from a key argument in boundary-layer theory: Prandtl's self-similar ansatz.

A. Self-similarity

Because of the y-independence, assumed in the Prandtl BL theory, the boundary layer flow is mathematically a 2D flow. Therefore the system of partial differential equations (4)–(6) for the BL flow can be reduced to ordinary differential equations (ODEs) by introducing a stream function Ψ. We do this differently from the usual procedure by including in its definition the density in order to automatically fulfil the continuity equation by construction.

$$\tilde{\rho}\, u_x = \frac{\partial\Psi}{\partial z}, \quad (8)$$

$$\tilde{\rho}\, u_z = -\frac{\partial\Psi}{\partial x}, \quad (9)$$

where $\tilde{\rho} \equiv \rho/\rho_m$ is the density nondimensionalized with $\rho_m = \rho(T_m, P_m)$. Apparently the continuity equation automatically follows from (8)–(9). Next, cf. Appendix B, we may introduce a self-similarity variable $\tilde{Z} \equiv z/\ell_c(x)$ and a similarity function $\tilde{\Psi}(\tilde{Z}) = \Psi(x,z)/(\ell_c(x)\, U_c)$, such that $\ell_c(x) = \sqrt{x\nu_m/U_c}$. Thus the velocity components are

$$u_x = U_c \frac{\tilde{\Psi}'}{\tilde{\rho}}, \quad u_z = \frac{\nu_m}{2\ell_c}\left\{\tilde{Z}\frac{\tilde{\Psi}'}{\tilde{\rho}} - \frac{\tilde{\Psi}}{\tilde{\rho}}\right\}, \quad (10)$$

with boundary conditions $\tilde{\Psi}(0) = 0 = \tilde{\Psi}'(0)$ and $\tilde{\Psi}'(\infty) = \tilde{\rho}_c$.

In terms of (10), the viscous BL equation (5) can be written as:

$$0 = \tilde{\eta}\tilde{\Psi}''' + \left\{\frac{1}{2}\tilde{\Psi} + \tilde{\eta}' - 2\frac{\tilde{\rho}'}{\tilde{\rho}}\tilde{\eta}\right\}\tilde{\Psi}''$$

$$+ \left\{-\frac{1}{2}\frac{\tilde{\rho}'}{\tilde{\rho}}\tilde{\Psi} + \left[2\left(\frac{\tilde{\rho}'}{\tilde{\rho}}\right)^2 - \frac{\tilde{\rho}''}{\tilde{\rho}}\right]\tilde{\eta} - \frac{\tilde{\rho}'}{\tilde{\rho}}\tilde{\eta}'\right\}\tilde{\Psi}(11)$$

Here $\tilde{\eta} \equiv \eta/\eta_m$ is the dimensionless viscosity, whose $\tilde{Z}$-dependence $\tilde{\eta}'$ is given by

$$\tilde{\eta}' = \left(\frac{\partial\tilde{\eta}}{\partial\tilde{\Theta}}\right)_{\tilde{\rho}}\tilde{\Theta}' + \left(\frac{\partial\tilde{\eta}}{\partial\tilde{\rho}}\right)_{\tilde{\Theta}}\tilde{\rho}',$$

where $\tilde{\Theta} \equiv (T - T_t)/\Delta$ denotes the dimensionless temperature.

Next, assuming that the pressure P_m is constant throughout the fluid, one finds

$$\tilde{\rho}' = -\tilde{\rho}\tilde{\beta}\tilde{\Theta}', \quad (12)$$

with $\tilde{\beta} \equiv \beta\Delta$. The boundary conditions at the respective walls are $\tilde{\rho}(0) = \tilde{\rho}_{b,t}$, $\tilde{\rho}'(0) = -\tilde{\rho}_{b,t}\tilde{\beta}_{b,t}\tilde{\Theta}'_{b,t}$, and $\tilde{\rho}(\infty) = \tilde{\rho}_c$.

Finally, we also write the temperature equation (6) in self-similar form as (see Appendix B 2)

$$\tilde{\Lambda}\tilde{\Theta}'' + \left\{\frac{1}{2}\tilde{c}_P \text{ Pr } \tilde{\Psi} + \tilde{\Lambda}'\right\}\tilde{\Theta}' = 0, \quad (13)$$

where $\tilde{\Lambda} \equiv \Lambda/\Lambda_m$ and $\tilde{c}_P \equiv c_P/c_{P,m}$. Equation (13) is subject to $\tilde{\Theta}(0) = \tilde{\Theta}_{b,t}$ and $\tilde{\Theta}(\infty) = \tilde{\Theta}_c$.

B. Results

The coupled ODEs (11)–(13) with the respective boundary conditions and the heat-flux conservation (7) are solved numerically with a shooting method [53]. The integration domain is restricted to Δ-intervals where the transport properties are concave/convex functions of the temperature. In particular, we have chosen ethane as the working fluid since its properties are known very well [47], even close to its critical point (T_*, P_*, ρ_*) [see figure 1]. All material properties $\eta, \Lambda, \rho, \beta$, and c_p are implemented in their full dependence on T In this manner, the computation of temperature and density profiles does not involve any fit parameter.

1. Vertical profiles

An insight into the structure of the BLs can be achieved by studying typical profiles along the z-direction. To describe them, let us consider a representative case in which the pressure is fixed at $P_m = 0.849 \cdot P_*$, the mean temperature at $T_m = 40\,°C$, and the thermal difference between the plates at $\Delta = 15$ K.

In figure 2, the temperature $\tilde{\Theta}$ and density $\tilde{\rho}$ are plotted as functions of the similarity variable $\tilde{Z}$. As shown in panel 2a, the center temperature $\tilde{\Theta}_c$ is *smaller* than the mean temperature $\tilde{\Theta}_m = 0.5$, clearly indicating a top-down symmetry breaking. Such symmetry breaking is also reflected in the density profiles shown in panel 2b, since the center density $\tilde{\rho}_c$ is *larger* than the mean density $\tilde{\rho}_m = 1$. Notwithstanding the pronounced curvatures in $\tilde{\Theta}(\tilde{Z})$ and $\tilde{\rho}(\tilde{Z})$, we shall restrict our attention
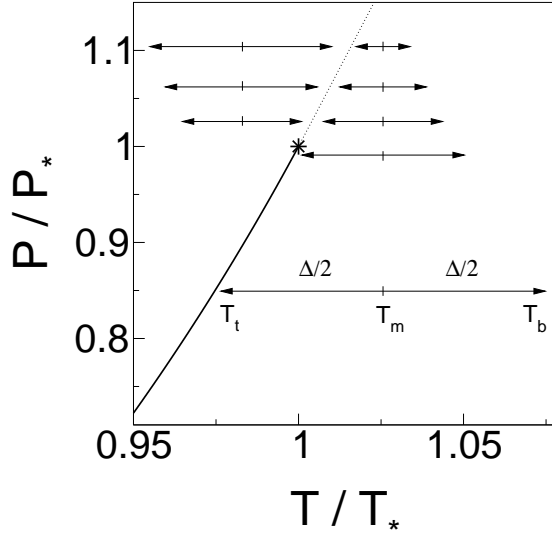
FIG. 1: Pressure-temperature plane in reduced units. Star: critical point of ethane ($T_* = 32.18°$C, $P_* = 48.718$ bar). Heavy line: liquid-vapor coexistence curve. Dotted line: critical isochore. The horizontal arrows show the maximum temperature intervals Δ, centered at $T_m = 27\,°$C (left) and $T_m = 40\,°$C (right). The pressures are $P_m/P_* = 0.849$, 0.991, 1.026, 1.062, and 1.104 (bottom to top).

to the *asymptotic* value $\tilde{\Theta}_c$ as a convenient indicator of NOB effects.

2. Center temperature

To compute the difference $T_c - T_m$ as a function of Δ, we have chosen a particular set of isobars in the phase diagram of ethane. As shown in figure 1, our selection of Δ-intervals falls into two classes: (i) those intervals centered at $T_m = 27\,°$C and (ii) those centered at $T_m = 40\,°$C.

As for the latter (the more gaseous case), figure 4a shows that the center temperature is a decreasing function of Δ. The top-down symmetry of the flow is broken in such a way that the top boundary layer tends to become thinner than its bottom counterpart, eventually leading to a temperature reduction in the center of the flow. Though this result has been originally reported and explained already in reference [46], we briefly mention it here for completeness of discussion.

Focussing now on the class of Δ-intervals centered at $T_m = 27°$ C, figure 4b shows that the center temperature becomes larger than the mean temperature between the plates. Such NOB effect is different to what we found in reference [46] and repeated in figure 4 a, where we have focused on the more gas-like case.

To understand this we argue that the intervals under consideration (centered at $T_m = 27°$ C) now correspond to a region of the phase diagram, where the material properties of ethane behave more similar to those of the
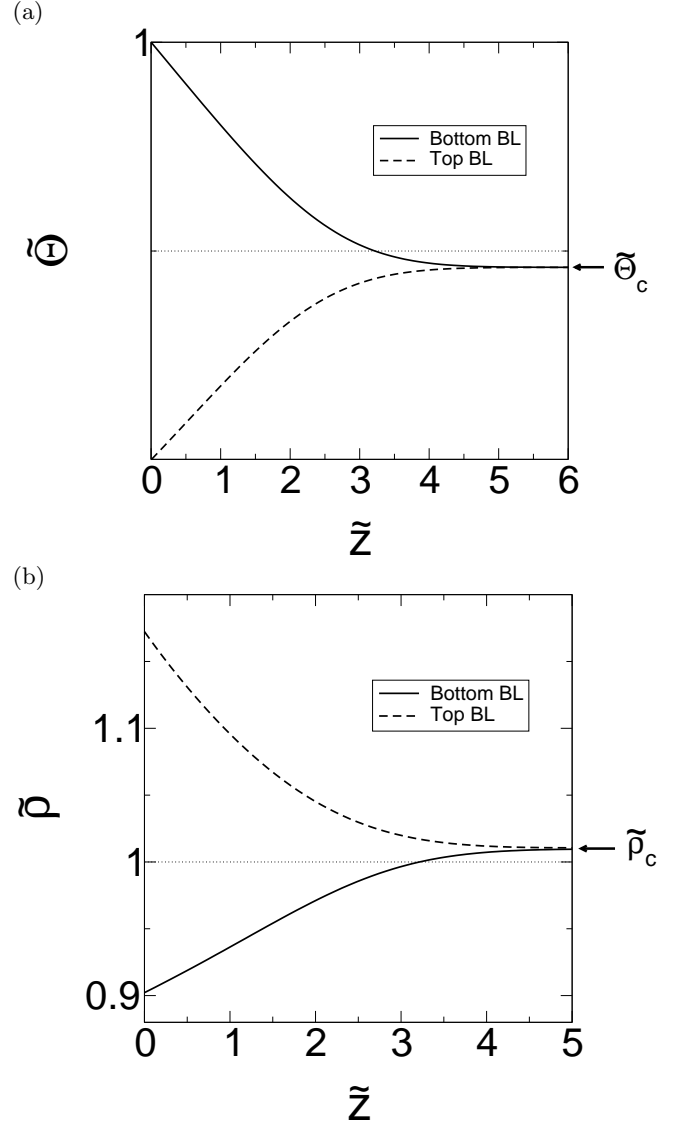

FIG. 2: (a) Temperature and (b) density profiles at $P_m = 0.849 \cdot P_*$, $T_m = 40°$ C and $\Delta = 15$ K. The thermal slope thicknesses at the bottom or top $\lambda_{b,t}^{sl}/L = a_{b,t}/\sqrt{\nu_m/LU_c}$ are seen to have prefactors of about $a_b \approx 2.8$ and $a_t \approx 2.5$, i.e., $\lambda_b^{sl} > \lambda_t^{sl}$.

liquid phase. NOB effects in classical liquids (such as water and glycerol) were already discussed in references [43, 44, 45]. One of our aims in the present work is to further assess the differences in the NOB effects between the more liquid-like versus the more gas-like fluids, see Sec. III. It will turn out that this will show us the limitations of boundary-layer theory, see Sec. IV. To this end, we first consider now additional experimental details on the Δ dependence of the center temperature $T_c(\Delta)$.

III. EXPERIMENT

A. Apparatus

The apparatus was described in detail before in Ref. [54], where a schematic diagram is shown in Fig. 2 . Here we give a brief description and details specific to the present high-pressure sample cell shown in Fig. 3. Working from the inside out, the sample cell was surrounded by a can containing ambient air. The air space inside the can was filled with low-density open-pore foam to prevent convection outside the sample. The maximum possible diameter of the sample top plate was 10 cm, allowing for inside sample diameters typically up to about $D = 8$ cm. The entire apparatus was of sufficient length to accommodate a sample with $L \simeq 16$ cm ($\Gamma \simeq 0.5$). Heat was applied at the sample bottom by a metal-film heater covering the entire active bottom-plate area uniformly.

The top plate was cooled by a circulating water bath. The water was cooled when passing through a heat exchanger external to the main apparatus which in turn was cooled by a separate water circuit driven by a Neslab or Lauda refrigerated circulator with a temperature stability of 0.01°C. Just before entering the apparatus, the water was heated by a heater consisting of about 25 m of teflon-insulated AWG30 (0.5 mm dia) copper wire, stuffed into the inlet line and thus immersed in the water. The large contact area between the water and the heater wire provided excellent heat exchange and uniform heating of the water. The heater was computer controlled in a feedback loop with a thermometer located in the top plate of the sample cell. The bath-temperature stability achieved in this way was a few tenths of a milli-Kelvin. The water entered the bottom center of the apparatus, flowed upward through an annular channel around the can, and was distributed over the top plate by a set of jets. With this arrangement the entire can was kept at the top-plate temperature and parasitic heat loss from the side wall and the bottom plate due to conduction through the air/foam as well as by radiation was reduced to a level that was negligible compared to the heat transport by the convecting fluid.

After cooling the top plate the water returned through an annular channel located just outside of and mildly insulated from the incoming channel. Since the water, while cooling the top plate, was never heated by more than a few mK, the returning water provided an excellent adiabatic thermal shield at the top-plate temperature, thus stabilizing the interior temperatures and preventing significant variations in time of the parasitic heat losses from the bottom plate. The entire apparatus sat on a chlorinated poly (vinyl chloride) (CPVC) base plate with appropriate channels and feed-throughs to accommodate the water circuit, the electrical leads, and the fill capillary going to the sample.

One of two high-pressure sample-cells (see Fig. 3) was installed inside the can. It had the shape of a cylin-
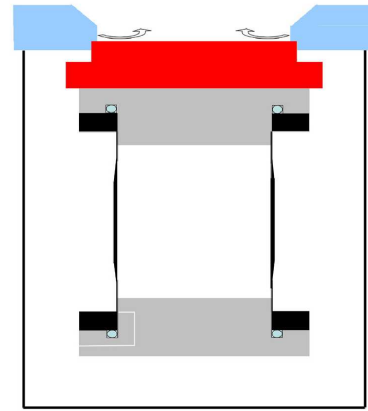

FIG. 3: Schematic diagram (approximately to scale for $\Gamma = 1$) of the high-pressure sample cell surrounded by the can containing ambient air and foam.

der with $D = 7.63$ cm. One cell had an internal length $L = 7.62$ cm, corresponding to an aspect ratio $\Gamma \equiv D/L = 1.00$. Another one had $L = 15.24$ cm, yielding $\Gamma = 0.500$. The top and bottom plates consisted of thick copper disks. Each of the two plates had an anvil, 1.59 cm thick, of diameter essentially equal to D, that was a close slide fit in the type 4340 steel side wall. After machining, the side wall was heat treated at 830°C and oil quenched. This procedure is expected to lead to a tensile strength of about 13 kbars. The side wall had a flange at each end, of thickness 0.95 cm. Each flange was bolted (not shown in the figure) and "O"-ring-sealed to one of the copper end plates. A top and bottom thin section of the side wall had a thickness of 0.051 (0.076) cm for the $\Gamma = 1$ ($\Gamma = 0.5$) cell. This thin section overlapped the copper anvils and extended into the sample region by 0.95 cm. Connecting the thin section was a central section of wall thickness 0.15 cm that provided enhanced strength; since the turbulent system contained only a very small thermal gradient in its center, the thicker wall section did not significantly enhance the wall heat-transport. The sample entered the bottom copper plate through a capillary from the side, and then proceeded through a very small hole (shown in white on the left side of the figure) into the gap between the bottom-plate anvil and the side wall.

The sample was connected to a manifold through a capillary. Also connected to the manifold was a separate pressure-regulation volume of 600 (1000) cm^3 in the case of the $\Gamma = 1$ ($\Gamma = 0.5$) cell that could be heated above the ambient temperature by a heater wrapped around its outside. The temperature of this "hot volume" was controlled in a feedback loop with a pressure gage [55]. The pressure stability typically was better that one milli-bar. The entire system was designed to safely withstand pressures up to 60 bars. For the pressure measurements we used a Paroscientific model 745 pressure standard with an accuracy or 80 ppm (about 6 milli-bars) and a reso-

lution of 1 ppm (about 70 micro-bars) of full scale.

A substantial fraction of the heat current passed through the side wall. This current was measured for the evacuated cell and subtracted from all other measurements; but as was recognized some time ago ([56, 57]), this is not an adequate procedure because of the height-dependent temperature gradients that prevail in the wall when the cell contains turbulently convecting fluid. We did not attempt a correction for this non-linear side-wall effect in the present case because we do not believe that a reliable correction is possible when the side-wall conductance is large. For this reason our values of Nu under OB condition are about 25% larger than other measurements at similar Prandtl numbers ([16]). However, we believe that the deviations of Nu and of T_c from their Boussinesq values, which (as we shall see below in Sect. III B 2) depend primarily on the nature of the top and bottom boundary layers rather than on the fluid interior, were obtained reliably.

The top and bottom temperatures T_t and T_b were determined from the average of six thermistors imbedded close to the fluid in each of the top and bottom plates ([58]). These thermistors were calibrated against a platinum-resistance thermometer purchased from Hart Scientific. This thermometer was supplied with a calibration, accurate to ± 7 mK, on the ITS90 temperature scale. The average temperature readings were used to obtain $\Delta = T_b - T_t$ and $T_m = (T_t + T_b)/2$. Small corrections for the temperature gradients in the copper plates were applied. The center temperature T_c was taken to be the average of the temperatures measured with eight thermistors attached to the outside of the side wall at the horizontal mid-plane, equally spaced in the azimuthal direction (see, for instance, Ref. [22] or [59]).

In order to obtain an estimate of the OB values of the Nusselt numbers, a power law $Nu_{OB} = N_0 R^{\gamma_{eff}}$ was fitted to the Nusselt-number measurements at relatively small Δ where $\beta_m \Delta \lesssim 0.05$, adjusting γ_{eff} and N_0. Such fits yielded values of γ_{eff} close to 0.30. All the measured values of Nu regardless of $\beta_m \Delta$ were then divided by the power-law value at the measured Rayleigh numbers to give Nu/Nu_{OB} at all Δ.

All measurements reported here were made with many values of Δ at each of a few constant values of T_m and P. In both cells we used ethane at elevated pressures as the fluid. The thermophysical properties were calculated from the formulas given in Ref. [47]. For extensive discussions of the uncertainties of these properties we refer to that paper. It is difficult to determine the absolute errors for the Rayleigh and Nusselt numbers that results from property uncertainties, but we expect that an estimate of a few percent is not unreasonable. Since in the present paper we are concerned only with the ratios Nu/Nu_{OB}, and since all data are taken as a function of Δ at a given mean temperature and pressure and evaluated at the same P and T_m, property errors cancel to a very large extent.
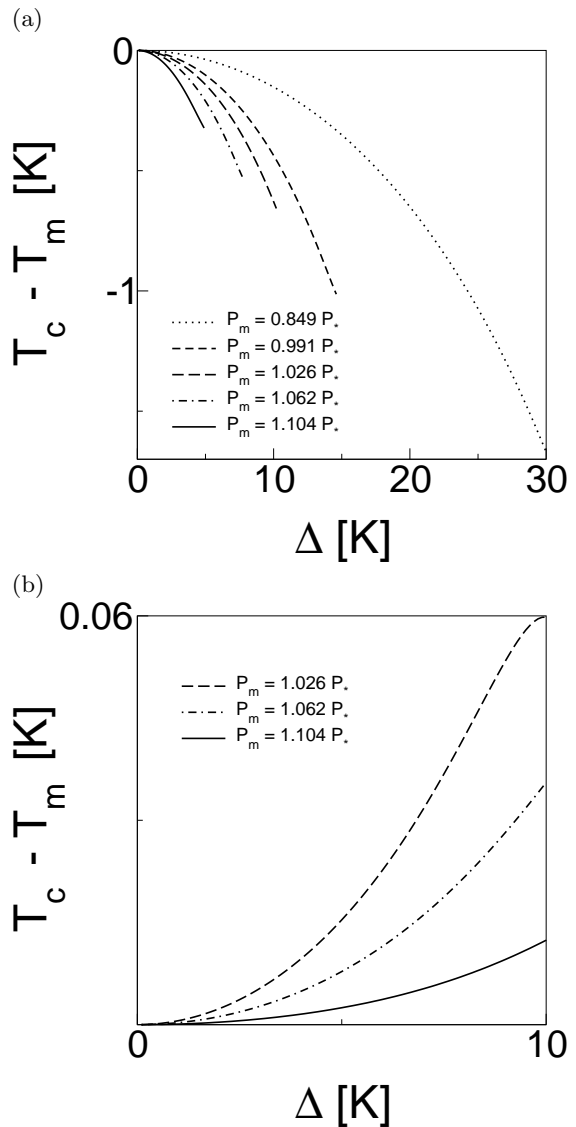

FIG. 4: Deviation $T_c - T_m$ as function of Δ, for (a) $T_m = 40\,^\circ$C and (b) $T_m = 27\,^\circ$C.

B. Results

1. The Nusselt number Nu(Ra)

As indicated above, we do not regard the results for Nu(Ra) to be very accurate because of unknown effects due to the relatively large wall conductivity. Nonetheless we show the results for $\Gamma = 1$ at several T_m and P in Fig. 5 on logarithmic scales. Over a wide range of Ra one sees that they are a few percent higher than the results from Refs. [6] and [7], and we attribute this to the influence of the side-wall conductivity on our data. At the largest Ra our results increase more rapidly with Ra, and data at different T_m and P begin to differ from each other. We attribute this phenomenon to NOB effects.
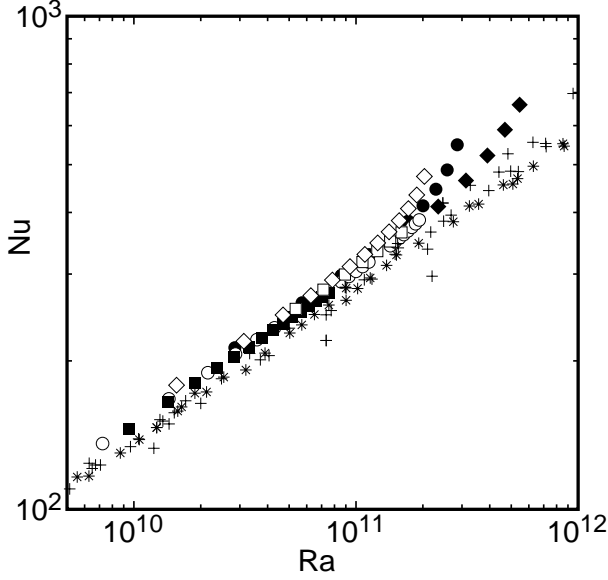
FIG. 5: (a): The Nusselt number Nu as a function of the Rayleigh number Ra for $\Gamma = 1.00$. Solid circles: $P = 51.72$ bars and $T_m = 40°$C (Pr = 2.58). Open circles: $P = 51.72$ bars and $T_m = 27°$C (Pr = 2.99). Solid squares: $P = 51.72$ bars and $T_m = 24°$C (Pr = 2.71). Open squares: $P = 51.72$ bars and $T_m = 31°$C (Pr = 3.85). Solid diamonds: $P = 53.79$ bars and $T_m = 40°$C (Pr = 3.79). Open diamonds: $P = 50.00$ bars and $T_m = 40°$C (Pr = 2.09). Stars: from Ref. [6] for $\Gamma = 0.5$ after correction for sidewall effects. Plusses: from Ref. [7] for $\Gamma = 0.5$.

FIG. 7: The ratios X/X_m for $P = 51.72$ bar ($P/P_* = 1.062$) of several property values X at temperatures $T - T_m$ to the value of X at T_m (based on Ref. [47]). (a) and (c): $T_m = 27.00°$C. (b) and (d): $T_m = 40.00°$C. (a) and (b): thermal conductivity Λ (short dashed line), density ρ (dotted line), and dynamic viscosity η (dash-dotted line). (c) and (d): thermal expansion coefficient β (solid line), $\hat{\beta}$ (long dashed line), and heat capacity at constant pressure c_P (double-dashed dotted line). The reference values X_m for 27(40)°C are $\Lambda_m = 0.07328(0.04343)$ W m^{-1} K^{-1}, $\rho_m = 331.12(123.26)$ kg m^{-3}, $\eta_m = 4.030(1.502)10^{-5}$ kg s^{-1} m^{-1}, $\beta_m = 0.01649(0.03815)$ K^{-1}, $c_{P,m} = 5434(7452)$ J kg^{-1} K^{-1} and mean Prandtl number $Pr_m = 2.99(2.58)$.

2. Aspect-ratio dependence

In Fig. 6 we compare results obtained at a mean temperature $T_m = 40.00°$C and pressure $P = 51.72$ bar ($P/P_* = 1.062$, Prandtl number $Pr = 2.58$) in the sample of aspect ratio $\Gamma = 0.50$ (open circles) with previously reported results ([46]) for $\Gamma = 1.00$ (solid circles). One sees that the NOB effect on Nu and on the center temperature T_c is within our resolution independent of Γ. This shows, as expected, that the NOB effects are confined essentially to the boundary layers. The length of the sample interior, which is nearly isothermal (see, however, Ref. [59]) regardless of its length, does not have a large influence.
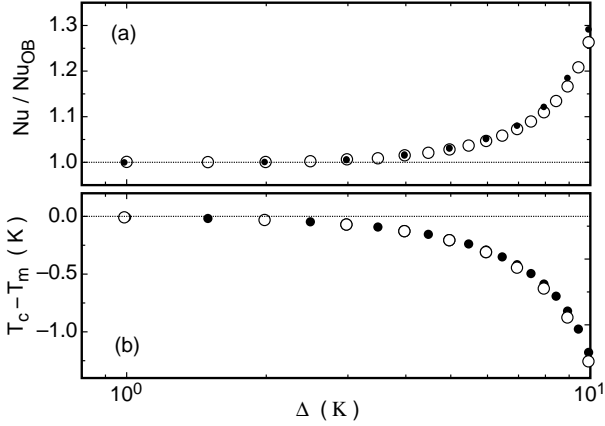

FIG. 6: (a): The ratio of the measured Nusselt number Nu to the estimate Nu_{OB} of the Nusselt number under Boussinesq conditions as a function of the applied temperature difference Δ. (b) The deviation of the center temperature T_c from the mean temperature T_m as a function of Δ. All measurements were made at $T_m = 40.00°$C and a pressure of 51.72 bar ($P/P_* = 1.062$) where the Prandtl number is 2.58. Open symbols: $\Gamma = 0.50$. Solid symbols: data from Ref. [46] with $\Gamma = 1.00$.
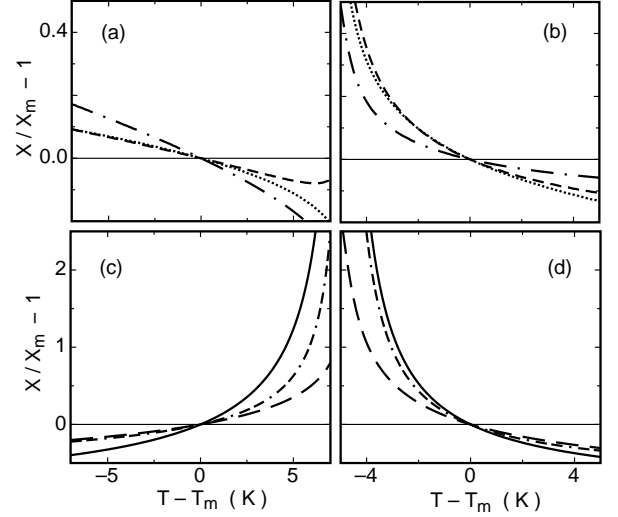
3. Dependence on fluid properties

Interesting insight into the influence of various property variations with temperature can be gained by measuring T_c and Nu along an isobar on the two sides of the temperature $T_\phi(P)$ at which the critical isochore is reached. In Fig. 7 we show the variation along the isobar $P = 51.72$ bar $= 1.062\,P_*$ of the thermal conductivity Λ,
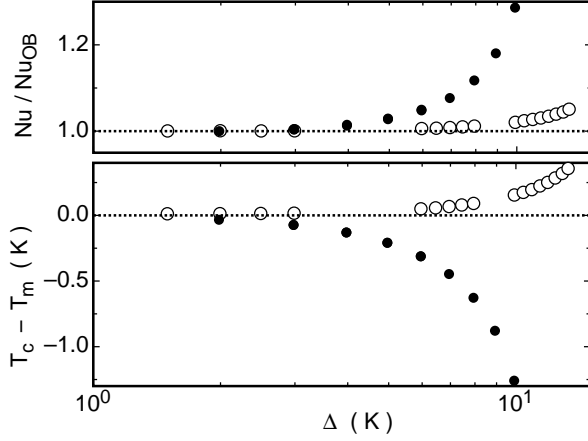
FIG. 8: (a): The ratio of the measured Nusselt number Nu to the estimate Nu_{OB} of the Nusselt number under Boussinesq conditions as a function of the applied temperature difference Δ. (b) The deviation of the center temperature T_c from the mean temperature T_m. These measurements were made for $\Gamma = 1.00$ at a pressure of 51.72 bar ($P/P_* = 1.062$). Open symbols: $T_m = 27.00°$C ($Pr = 2.99$). Solid symbols: $T_m = 40.00°$C ($Pr = 2.58$). These two temperatures are on opposite sides of, but not equidistant from, the temperature $T_\phi = 34.97°$C where the critical isochore is reached on this isobar.
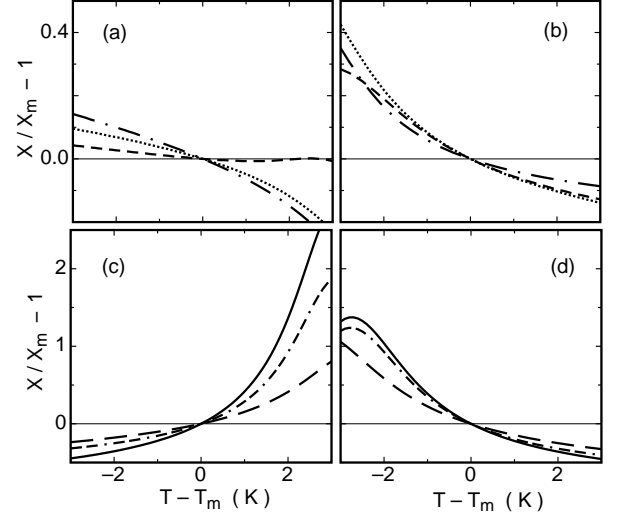

FIG. 9: The ratios X/X_m for $P = 55.17$ bar ($P/P_* = 1.132$) of several property values X at temperatures $T - T_m$ to the value of X at T_m (based on Ref. [47]). (a) and (c): $T_m = 35.00°$C. (b) and (d): $T_m = 41.00°$C. (a) and (b): thermal conductivity Λ (dashed line), density ρ (dotted line), and dynamic viscosity η (dash-dotted line). (c) and (d): thermal expansion coefficient β (solid line), $\hat{\beta}$ (long dashed line), and heat capacity at constant pressure c_P (double-dashed dotted line). The reference values X_m for 35(41)°C are $\Lambda_m = 0.06674(0.05163)$ W m^{-1} K^{-1}, $\rho_m = 282.48(153.43)$ kg m^{-3} $\eta_m = 3.168(1.726)10^{-5}$ kg s^{-1} m^{-1}, $\beta_m = 0.04177(0.06876)$ K^{-1}, $c_{P,m} = 9617(12534)$ J kg^{-1} K^{-1}, and mean Prandtl number $Pr_m = 4.56(4.20)$.

density ρ, dynamic viscosity η, thermal expansion coefficient β, and heat capacity c_P for the cases $T_m = 27.00°$C (left panels) and 40.00°C (right panels). These two values are on opposite sides of but not quite equi-distant from $T_\phi = 34.97°$C. In the upper two panels one sees that the variations of Λ, ρ, and η are relatively small, have the same trends with T though quantitatively they are somewhat different on the two sides, with maximum changes by less than a factor of two over temperature ranges that are small enough to avoid including T_ϕ. On the other hand, the expansion coefficient and the heat capacity (lower two panels) vary by a factor of five or more. Thus one might expect them to dominate the NOB effects. Interestingly they have opposite trends with $T - T_m$, the temperature derivatives of both β and c_P are positive below and negative above T_ϕ; that is below the critical isochore (along the temperature axis), on the more liquid-like side, β and c_P are smaller at the top (colder) than at the bottom (warmer) end of the sample, with this relationship reversed above the critical isochore, on the more gas-like side, where β and c_P decrease from bottom to top.

In Fig. 8 experimental results are presented for $\Gamma = 1.00$ at a pressure $P = 51.72$ bar $= 1.062$ P^*. They are for the two mean temperatures $T_m = 27.00$ (open circles) and 40.00°C (solid circles) of Fig. 7 where the Prandtl numbers are 2.99 and 2.58 respectively. In both cases we used Δ values sufficiently small so that T_t (T_b) only reaches down (up) to T_ϕ so that the applied temperature

difference does not straddle T_ϕ. One sees that the NOB effects increase Nu on both sides of the critical isochore. On the high-temperature side (solid circles) the NOB effect is larger for the same Δ. This is consistent with the larger variation of the fluid properties at equal values of $T - T_m$ revealed above in Fig. 7.

The NOB effect on T_c is of *opposite* sign on the two sides of the critical isochore. For $T < T_\phi$ (open circles) NOB conditions increase T_c above T_m, whereas for $T > T_\phi$ (solid circles) T_c is reduced below T_m. This observation, in conjunction with the properties shown in Fig. 7, suggests that for these fluids the temperature drops $\Delta_{t,b}$ across the boundary layers are determined primarily by β and/or c_P, with $\Delta_t > \Delta_b$ ($\Delta_t < \Delta_b$) when β and/or c_P are smaller (larger) at the cold top end of the sample then at the warm bottom end. As pointed out before, [43] for the Nusselt number the contributions to the thermal resistance at the two boundary layers add, and it does not matter much whether the larger or smaller contribution comes from one end or the other. Thus, for Nu the NOB effect is in the same direction in both cases. As was the case for Nu, the NOB effect revealed by T_c is larger in magnitude above T_ϕ than it is below. Again we attribute this difference primarily to the difference in the variations of the properties shown in Fig. 7.
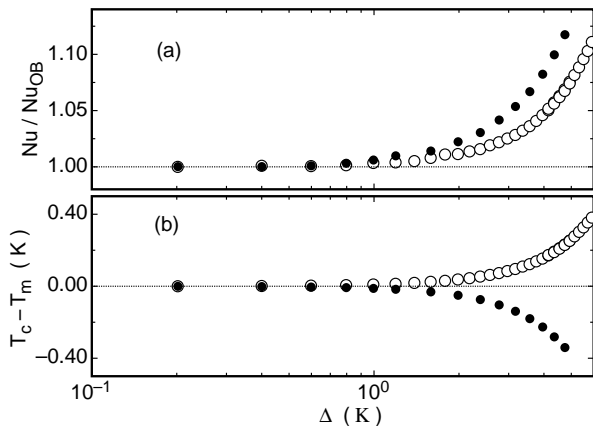
FIG. 10: (a): The ratio of the measured Nusselt number Nu to the estimate Nu_{OB} of the Nusselt number under Boussinesq conditions as a function of the applied temperature difference Δ. (b) The deviation of the center temperature T_c from the mean temperature T_m. These measurements were made for $\Gamma = 0.50$ at a pressure of 55.17 bar ($P/P_* = 1.132$). Open symbols: The mean temperature $T_m = 35°$C ($Pr = 4.56$). Solid symbols: $T_m = 41°$C ($Pr = 4.20$). These two temperatures are on opposite sides of and nearly equidistant from the temperature $T_\phi = 38.06°$C where the critical isochore is reached on this isobar.

In Fig. 9 we show the variation along the isobar $P = 55.17$ bar ($P/P_* = 1.132$) of the various properties for the cases $T_m = 35.00°$C (left panels) and $41.00°$C (right panels). These two temperatures are also on opposite sides of and nearly equi-distant from the critical isochore, for this pressure at $T_\phi = 38.06°$C. Again the variation of the expansion coefficient and the heat capacity (lower two panels) is much larger than that of the other properties. At a given $|T - T_m|$, all the variations are more similar in magnitude on the two sides of T_ϕ than they were for the case of Fig. 7.

In Fig. 10 experimental results corresponding to the conditions of Fig. 9 are presented for $\Gamma = 0.50$. They are for the two mean temperatures $T_m = 35.00$ (open circles) and $41.00°$C (solid circles) where the Prandtl numbers are 4.56 and 4.20 respectively. In both cases we used $\Delta \leq 6$ K so that T_t (T_b) reaches down (up) to T_ϕ when $T_m = 41°$C ($35°$C) while the applied temperature difference does not straddle T_ϕ. For this case one sees that the NOB effects on Nu are similar on the two sides of the critical isochore. Again, the NOB effect on T_c, although of about the same magnitude, is of opposite sign on the two sides. For $T < T_\phi$ (open circles, more liquid-like) NOB conditions increase T_c above T_m, whereas for $T > T_\phi$ (solid circles, more gas-like) T_c is reduced below T_m.

IV.   COMPARISON BETWEEN BOUNDARY-LAYER THEORY AND THE EXPERIMENTAL RESULTS

We now compare the experimental measurements from the previous section with the boundary layer results presented in section II. In particular, since the comparison with experiments at $T_m = 40°$ C (more gas-like ethane) was already discussed in reference [46], finding good agreement between experiment and the extended BL theory, we devote special attention to the new measurements at $T_m = 27°$ C and $P/P_* = 1.062$ (more liquid-like ethane).

As shown in figure 11, the curve for more liquid-like ethane obtained from BL theory considerably deviates from the experimental data. This is remarkably different from the comparison of BL theory with gaseous ethane, presented in [46], where instead a good agreement was observed. This suggests that even though BL theory reasonably captures NOB effects associated with (OB.1) and (OB.2), further corrections are essential in the present liquid-like ethane case. Among them, deviations from (OB.3) seem to be the natural candidate for the failure of BL theory, since the buoyancy force is *not* included in the BL equations but apparently affects the thermal convection. Thus, in order to reveal the importance of nonlinear buoyancy in thermal convection, we shall perform direct numerical simulations (DNS) of the RB problem.

V.   DIRECT NUMERICAL SIMULATIONS

As shown in refs. [45, 60], two-dimensional direct numerical simulations may be useful for the study of the tiny NOB effects which occur in RB convection in liquids. In particular, even with the restrictions to two-dimensional geometry and to incompressibility of the fluid flow, the effects on the center temperature and the Nusselt number shift could be reasonably captured in the cases of water and glycerol. However, the liquid-like ethane just above the critical pressure has a stronger temperature dependence of the density than water and glycerol. To quantify this, a comparison between the ethane properties around $T_m = 27°$C and $P/P_* = 1.062$ with water and glycerol around $T_m = 40°$C is reported in figure 12. For the case of ethane the incompressible flow approximation seems to be questionable, or at least less justified. But we will show that adopting the same approach used for water and glycerol [45, 60] also proves to be useful to study NOB effects in ethane and the results are well consistent with experiment.

Further insight into the problem is given by considering several cases of artificial ethane-like fluids, namely fluids which have only one, or some, of their material properties dependent on temperature, while the others are kept constant. In particular, as discussed in the previous section, we will examine the relevance of the nonlinear temperature dependence of buoyancy on the center tem-
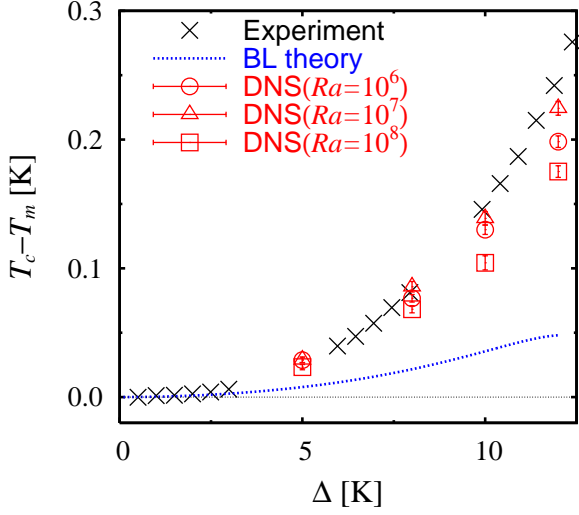
FIG. 11: Deviation $T_c - T_m$ as function of Δ, for $T_m = 27\,^\circ$C and $P/P_* = 1.062$. The symbols ($\times$) correspond to experimental measurements. The dotted line is obtained from boundary layer theory. The red symbols ($\bigcirc$, $\triangle$, and $\square$) with error bars correspond to the incompressible DNS results described in section V, measured at different $Ra = 10^6$ to $Ra = 10^8$. Note that though these Rayleigh numbers are smaller than in the experiments ($Ra = O(10^9)$-$O(10^{10})$), the comparison is still appropriate because the T_c shift has proven to be rather independent of Ra for given Δ, provided one is beyond the onset of the chaotic motion at $Ra \approx 2 \cdot 10^5$ [45, 60]. For further evidence for the weak Ra-dependence of the center temperature we also refer to table II.

perature shift $T_c - T_m$ and take full notice of violating OB.3, which in contrast assumes constant $\partial\rho/\partial T$. We remind that this cannot be taken into account in the extended BL theory presented in section II, while DNS can well include it.

A. Numerical simulation approach

To handle the numerical effort we restrict ourselves to incompressible and even two dimensional flow. The equations governing non-Oberbeck-Boussinesq convection in incompressible fluid flow are the incompressibility condition

$$\partial_i u_i = 0 \, , \tag{14}$$

the Navier-Stokes equation

$$\rho_m(\partial_t u_i + u_j \partial_j u_i) = -\partial_i p + \partial_j(\eta(\partial_j u_i + \partial_i u_j))$$
$$+ g\rho_m \left(1 - \rho/\rho_m\right)\delta_{i3}, \tag{15}$$

and the heat-transfer equation

$$\rho_m c_{p,m}(\partial_t T + u_j \partial_j T) = \partial_j(\Lambda \partial_j T). \tag{16}$$

Here, δ_{i3} is the Kroneker symbol. The density is assumed to be constant and its value ρ_m is fixed at that
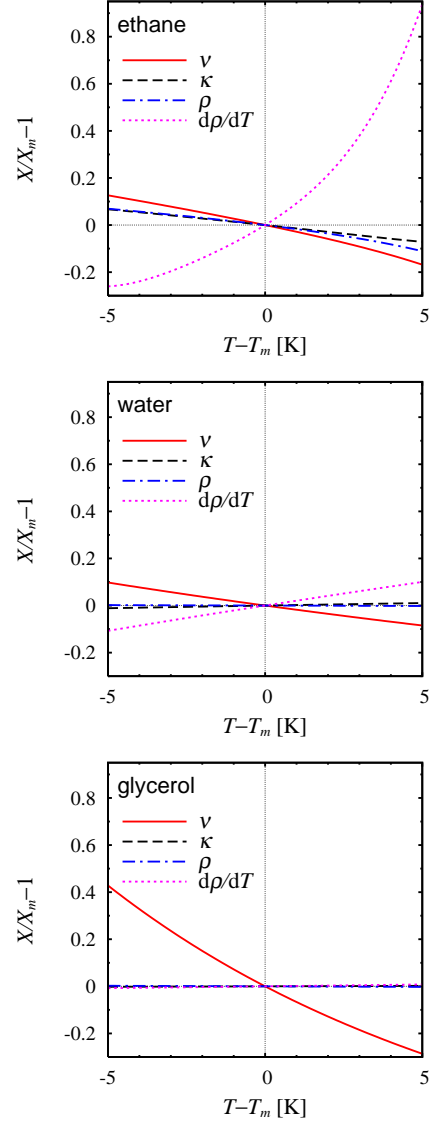

FIG. 12: Temperature dependences of the material properties ν, κ, ρ in the relevant T-range. $d\rho/dT$ is also displayed. (a) Ethane around the temperature $T_m = 27\,^\circ$C adapted from [47]. The pressure is $P/P_* = 1.062$. (b) and (c): The fluid properties for water (b) and glycerol (c), respectively, around the temperature $T_m = 40\,^\circ$C (which has been studied in [45] and [60]). Note the significant variation of the density ρ with T in the case of ethane, as compared to the two liquids. In ethane, $\rho/\rho_m - 1$ various from about 0.07 for $T - T_m = -5K$ to about -0.1 for $T - T_m = +5K$, whereas in glycerol ρrho_m is practically independent of T. The strong variation of ρ for ethane follows from the large $d\rho/dT$ (also shown).

of the temperature T_m, except in the buoyancy term, where the full nonlinear temperature dependence of $\rho(T)$ is implemented. The dynamic viscosity $\eta(T)$ and the heat conductivity $\Lambda(T)$ are also both temperature and thus space dependent. The isobaric specific heat capacity c_P is assumed to be constant, its value being $c_{p,m}$

(in contrast to real ethane). The experimentally known temperature dependences of ρ, η, Λ and the values of the parameters ρ_m, $c_{p,m}$ for ethane are given in [47] and, for better reference, are reported in Table I in the specific form implemented in our DNS.

For consistency with the experimental measurements and with the BL theoretical analyses presented above for liquid-like ethane, we chose the arithmetic mean temperature to be $T_m = 27°C$ and the pressure as $P/P_* = 1.062$.

B. Numerical results: T_c shift in liquid-like ethane

From figure 11 we can conclude that the DNS captures the experimental measurements of the center temperature shift $T_c - T_m$ as a function of Δ quite reasonably. The quality of the agreement with the available ethane data is similar to the one we have observed for glycerol [45] and for water [60]. This also serves as a further validation of our numerical approach.

We note that for water and for glycerol the T_c shift obtained by the extended BL theory [43] is nearly the same as calculated by DNS (see [45, 60]). In contrast, for the liquid-like ethane, the extended and even compressible BL theory only provides the right trend in the shift, but can not capture its amplitude (see again Fig. 11). This observation supports our guess on the relevance of the nonlinear T-dependence of $\rho(T)$ and thus of buoyancy. This latter is fully included in the DNS, as described in the previous subsection, while in BL theory it cannot be taken care of.

One of the advantages of the DNS as compared to real experiments is that the material properties are easily and independently tunable. Therefore, the dynamics of *hypothetical ethane-like liquids* can also be addressed. In the next subsection we shall see how this approach is useful in understanding the effects of the temperature dependence of the various material properties on the center temperature shift.

C. T_c shift in hypothetical fluids

To obtain more insight into the physical origin of the non-Oberbeck-Boussinesq T_c-shift, we consider NOB corrections for hypothetical ethane-like fluids in which at least one of the temperature dependences of $\kappa(T)$, $\nu(T)$, $\hat{\beta}(T)$ is switched off, and fixed at the OB values κ_m, ν_m, β_m. The quantity $\hat{\beta}(T)$, defined in eq. (2), is useful for the classification of the hypothetical fluids discussed in the following sections, but $\hat{\beta}(T)$ is not explicitly introduced into the DNS, in which the density difference $\rho(T) - \rho_m$ is taken instead, see Eq.(15) and Tab. I. Finally, we remind that $\hat{\beta}(T) = \beta_m$, the usual thermal expansion coefficient, if the fluid density is a *linear* function of the temperature around T_m (i.e., if the conditions
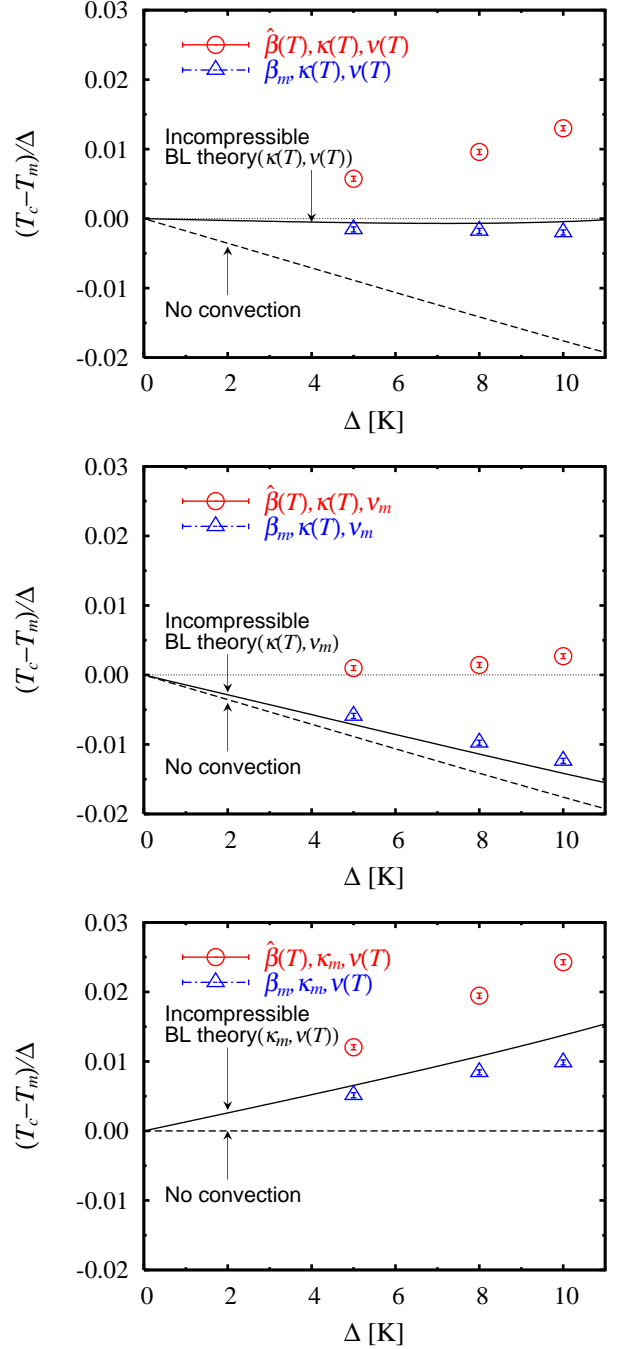

FIG. 13: The normalized center temperature shift $(T_c - T_m)/\Delta$ versus the temperature difference Δ for several hypothetical liquids. We consider the following six hypothetical liquids: $(\hat{\beta}(T), \kappa(T), \nu(T))$, $(\beta_m, \kappa(T), \nu(T))$, $(\hat{\beta}(T), \kappa(T), \nu_m)$, $(\beta_m, \kappa(T), \nu_m)$, $(\hat{\beta}(T), \kappa_m, \nu(T))$ and $(\beta_m, \kappa_m, \nu(T))$. In particular in each panel we compare two cases, which differ only by their buoyancy's T-dependence, i.e., $\hat{\beta}(T)$ instead of β_m. The symbols indicate the simulation results at Rayleigh number $Ra = 10^6$. The circles ($\bigcirc$) correspond to the cases in which the full temperature dependence of the buoyancy $(T - T_m)\hat{\beta}(T)$ is taken into account, while the triangles ($\triangle$) represent the cases where only the linear temperature dependence $(T - T_m)\beta_m$ is considered. The solid line shows the prediction of boundary layer theory with an incompressible flow assumption [43]. The dashed line stems from the solution with no convective flow $\partial_z(\kappa(T)\partial_z T) = 0$ with boundary conditions $T = T_b$ at $z = 0$ and $T = T_t$ at $z = L$. See also Table II.

| n | ν | κ | $g(1-\rho/\rho_m)$ |
	A_n	B_n	C_n
0	$1.21734 \cdot 10^{-7}$ [m^2/s]	$4.07547 \cdot 10^{-8}$ [m^2/s]	
1	$-3.38861 \cdot 10^{-9}$ [m^2/(s K)]	$-5.77921 \cdot 10^{-10}$ [m^2/(s K)]	$1.64833 \cdot 10^{-2}$ [m/(s^2 K)]
2	$-8.30683 \cdot 10^{-11}$ [m^2/(s K^2)]	$-7.36395 \cdot 10^{-12}$ [m^2/(s K^2)]	$6.79967 \cdot 10^{-4}$ [m/(s^2 K^2)]
3	$-5.75280 \cdot 10^{-12}$ [m^2/(s K^3)]	$-9.06743 \cdot 10^{-14}$ [m^2/(s K^3)]	$4.53854 \cdot 10^{-5}$ [m/(s^2 K^3)]
4	$-7.64359 \cdot 10^{-13}$ [m^2/(s K^4)]	$1.49555 \cdot 10^{-13}$ [m^2/(s K^4)]	$6.13485 \cdot 10^{-6}$ [m/(s^2 K^4)]
5	$-8.70191 \cdot 10^{-14}$ [m^2/(s K^5)]	$2.56836 \cdot 10^{-14}$ [m^2/(s K^5)]	$6.94645 \cdot 10^{-7}$ [m/(s^2 K^5)]

TABLE I: Expansion coefficients of material properties of ethane around the temperature $T_m = 27°$C adapted from [47]. The pressure normalized by its critical value is $P/P_* = 1.062$. The *effective* kinematic viscosity, the *effective* thermal diffusivity, and the buoyancy are written in a polynomial form as $\nu(T) \equiv \eta(T)/\rho_m = \sum_{n=0} A_n(T - T_m)^n$ [m^2/s], $\kappa(T) \equiv \Lambda(T)/(\rho_m c_{p,m}) = \sum_{n=0} B_n(T - T_m)^n$ [m^2/s], and $g(1 - \rho(T)/\rho_m) = \sum_{n=1} C_n(T - T_m)^n$ [m/s^2], respectively. Using the leading coefficient for the buoyancy force, we can write the Rayleigh number as $Ra = \beta_m L^3 \Delta/(\nu_m \kappa_m)$, where $\beta_m = C_1$, $\nu_m = A_0$ and $\kappa_m = B_0$, which coincides with the usual OB definition. The polynomial expensions for $\beta(T)$ and $\hat{\beta}(T)$ are $g\hat{\beta}(T) = \sum_{n=1} C_n(T - T_m)^{n-1}$ and $g\beta(T) = (\rho_m/\rho(T)) \cdot \sum_{n=1} nC_n(T - T_m)^{n-1}$.

OB.3 holds). In that case the thermal expansion coefficient $\beta(T) = \beta_m/[1 - (T - T_m)\beta_m]$ still depends on T unless $\beta\Delta \ll 1$.

For convenience hereafter we will call the two classes of artificial fluids, based respectively on the full non-linear NOB buoyancy force and on the linear OB approximation as defined by OB.3, as the $\hat{\beta}(T)$-fluids and β_m-fluids.

In figure 13 we present the DNS results of the normalized temperature shift $(T_c - T_m)/\Delta$ for several types of hypothetical fluids. The numeral values are given in table II. One clearly observes in the figures and in the table that the temperature dependence of the thermal expansion function $\hat{\beta}(T)$ apparently is relevant for the shift of T_c. What can also be noticed in particular from table II is that the corrections of the center temperature originating from the temperature dependence of either ν, κ, or β are approximately additive (i.e., add "linearly"): E.g., the center temperature corrections of the fluids with (β_m, κ_m, $\nu(T)$) and with (β_m, $\kappa(T)$, ν_m) add to that of the fluid with (β_m, $\kappa(T)$, $\nu(T)$), etc. Note that this additivity is in contrast to what had been found within the extended BL theory of ref. [45] where the full compressibility of the density had been taken into consideration. Instead, in DNS we have restricted to incompressible flow.

1. $\hat{\beta}(T)$- and β_m-fluids and extended BL

In figure 13 we also compare fluids of $\hat{\beta}(T)$- and β_m-type with equal properties of thermal conductivity and kinematic viscosity on the different panels. For convenient comparison the predictions by the extended BL theory under the assumption of fluid incompressibility [43] are also shown for the hypothetical fluids. Note that in such case the chosen type of buoyancy force needs not be specified, because BL theory does not capture it: For the BL theory $\hat{\beta}(T)$- and β_m-ethane are not distinguishable with respect to buoyancy. As a reference, the T_c-shift value in the purely conductive case ($u_i = 0$ everywhere)

is also reported. The T_c shift in this case is not zero for fluids with $\kappa = \kappa(T)$ as a result of the solution of the heat conduction equation $\kappa \, \partial_z^2 T + \frac{\mathrm{d}\kappa}{\mathrm{d}T}(\partial_z T)^2 = 0$ with $\frac{\partial \kappa}{\partial T}|_P \neq 0$.

We now discuss our main findings. The change in T_c for the hypothetical liquids with β_m relative to the ones with $\hat{\beta}(T)$ is comparable for given Δ. More importantly, we find that the deviation $(T_c - T_m)/\Delta$ calculated with DNS is well captured by the BL theory for the cases of artificial β_m-fluids, i.e., for fluids where $\rho(T)$ is assumed to be a linear function of T. In contrast, BL theory is always far from the T_c shift obtained for the more real $\hat{\beta}(T)$-ethane. This indicates that the extended BL theory well captures the NOB effect once the assumption (OB.3) is satisfied, even if (OB.1) and (OB.2) are violated, but it does *not* correctly describe the NOB effects, if (OB.3) is violated. Furthermore, the DNS results reveal that the T_c-shift is always enhanced if a temperature dependence of the thermal expansion function $\hat{\beta}(T)$ determines the buoyancy, i.e., if $\rho(T)$ depends nonlinearly on T.

2. Mirror transformation $\hat{\beta}(T) \rightarrow \hat{\beta}(2T_m - T)$

To quantitatively appreciate the effect of the temperature dependence in each material property individually also at different Rayleigh numbers, $Ra = 10^6$-10^8, we list the T_c shifts for several hypothetical ethane-like fluids in Tab. II. Since here our primary concern is the influence of the thermal expansion function, besides the $\hat{\beta}(T)$- and β_m-fluids a new class of hypothetical fluids is introduced. We consider $\hat{\beta}(2T_m - T)$-fluids obtained by the mirror transformation $\hat{\beta}(T) \rightarrow \hat{\beta}(2T_m - T)$. As schematically shown in figure 14, this transformation reverts the non-linearity in the buoyancy force with respect to $T - T_m$. The comparison between the cases $(\hat{\beta}(T), \kappa_m, \nu_m)$ and $(\hat{\beta}(2T_m - T), \kappa_m, \nu_m)$ - cases 4 and 8 in table II - shows that the effect of the mirror transformation on the out-

case	$\hat{\beta}$	κ	ν	$100(T_c - T_m)/\Delta$ at $Ra = 10^6$	$100(T_c - T_m)/\Delta$ at $Ra = 10^7$	$100(T_c - T_m)/\Delta$ at $Ra = 10^8$
1 (NOB)	$\hat{\beta}(T)$	$\kappa(T)$	$\nu(T)$	1.3003 ± 0.0369	1.3879 ± 0.0527	1.0788 ± 0.0362
2	$\hat{\beta}(T)$	$\kappa(T)$	ν_m	0.2699 ± 0.0356	0.2174 ± 0.0515	0.1251 ± 0.0414
3	$\hat{\beta}(T)$	κ_m	$\nu(T)$	2.4283 ± 0.0361	2.4351 ± 0.0496	2.4370 ± 0.0462
4	$\hat{\beta}(T)$	κ_m	ν_m	1.4805 ± 0.0355	1.4320 ± 0.0735	1.3796 ± 0.0534
5	$\hat{\beta}(2T_m - T)$	$\kappa(T)$	$\nu(T)$	-1.5953 ± 0.0361	-1.7946 ± 0.0506	-1.5868 ± 0.0320
6	$\hat{\beta}(2T_m - T)$	$\kappa(T)$	ν_m	-2.6382 ± 0.0357	-2.7458 ± 0.0496	-2.5516 ± 0.0496
7	$\hat{\beta}(2T_m - T)$	κ_m	$\nu(T)$	-0.4738 ± 0.0375	-0.4578 ± 0.0580	-0.3358 ± 0.0354
8	$\hat{\beta}(2T_m - T)$	κ_m	ν_m	-1.4878 ± 0.0366	-1.5358 ± 0.0504	-1.4013 ± 0.0363
9	β_m	$\kappa(T)$	$\nu(T)$	-0.1983 ± 0.0361	-0.2043 ± 0.0467	-0.2691 ± 0.0587
10	β_m	$\kappa(T)$	ν_m	-1.2369 ± 0.0363	-1.1883 ± 0.0611	-1.1851 ± 0.0369
11	β_m	κ_m	$\nu(T)$	0.9852 ± 0.0364	1.0834 ± 0.0576	0.9916 ± 0.0259
12 (OB)	β_m	κ_m	ν_m	0.0171 ± 0.0381	-0.0484 ± 0.0548	0.0271 ± 0.0387

TABLE II: DNS results for the center temperature shift $T_c - T_m$ normalized by the temperature difference $\Delta = 10$K for several hypothetical fluids. The *effective* thermal expansion function is given by $\hat{\beta}(T) = g^{-1} \sum_{n=1} C_n (T - T_m)^{n-1}$ [1/K]. Using the expansion coefficients C_n listed in Table I, we write the buoyancy for the case of $\hat{\beta}(2T - T_m)$ as $g(1 - \rho(T)/\rho_m) = \sum_{n=1} (-1)^{n+1} C_n (T - T_m)^n$ [m/s^2], and in the β_m case as $g(1 - \rho(T)/\rho_m) = C_1 (T - T_m)$ [m/s^2]. Although the center temperature shift for the OB case (case 12) should be essentially zero due to the top-bottom symmetry, the mean value determined from the DNS result is non-zero since the sampling time for taking the statistics is finite. Note that measurements of the temperature shift in the OB case are all, within statistical uncertainty, compatible with zero.
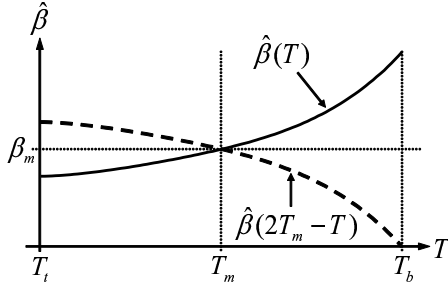

FIG. 14: Schematic plot of the mirror transformation $\hat{\beta}(T) \to \hat{\beta}(2T_m - T)$ of the thermal expansion coefficient $\hat{\beta}$.

put parameter T_c is to change the sign of $(T_c - T_m)/\Delta$ while preserving its modulus. Furthermore, the deviation of $(T_c - T_m)/\Delta$ for all β_m-fluids (cases 9,10,11) relative to the $\hat{\beta}(T)$-fluids (cases 1,2,3) is always positive, while it is always negative relative to the $\hat{\beta}(2T_m - T)$-fluids (cases 5,6,7). These features hold at all the studied Ra numbers. Therefore, we conclude that the shift $T_c - T_m$ is sensitive to the sign of the slope of $\hat{\beta}(T)$ or, equivalently, to the sign of the nonlinear term in the buoyancy factor $1 - \rho(T)/\rho_m$. More precisely speaking, the mirror transformation changes the signs of the even order coefficients C_2 and C_4 defined in Tab. I. Obviously C_2 is the larger and thus the most relevant coefficient. These features are absent in water and in glycerol, because for those the temperature dependence of $\rho(T)$ is much less pronounced.

3. Test on the linearity of the $T_c - T_m$ shift

Looking at Tab. II in more detail we find that all changes in $(T_c - T_m)/\Delta$, which stem from the nonlinear T-dependence of the buoyancy force, i.e., from the differences between β_m and $\hat{\beta}(T)$ (or $\hat{\beta}(2T_m - T)$) but having the same temperature dependences of κ and ν, are comparable. To emphasize this feature, we look at the differences $T_c|_{\hat{\beta}(T)} - T_c|_{\beta_m}$ (or $-(T_c|_{\hat{\beta}(2T_m - T)} - T_c|_{\beta_m})$) and plot them versus Δ as well as versus Ra, see figure 15. We find a good collapse of the data onto a single curve for various temperature dependences of κ and ν. In particular, the comparison between the middle and bottom panels of Fig. 15 leads to the relation $T_c|_{\hat{\beta}(T)} - T_c|_{\beta_m} = -(T_c|_{\hat{\beta}(2T_m - T)} - T_c|_{\beta_m})$, which indicates that the T_c change is dominated by the quadratic term in $1 - \rho(T)/\rho_m$, but is almost independent of κ and ν. This observation may be important for further attempts to improve the extended NOB BL theory.

VI. CONCLUSIONS

In this paper we have first presented in full detail the extension of boundary-layer theory to the case of compressible NOB fluids in a Rayleigh-Bénard system. The theory predicts a deviation of the center temperature T_c from the arithmetic mean temperature T_m between the top and bottom plates, i.e., $T_c - T_m \neq 0$.

Second, the theory has been tested against new experimental data for ethane near the critical point in its more liquid-like phase. Data come from a series of experiments
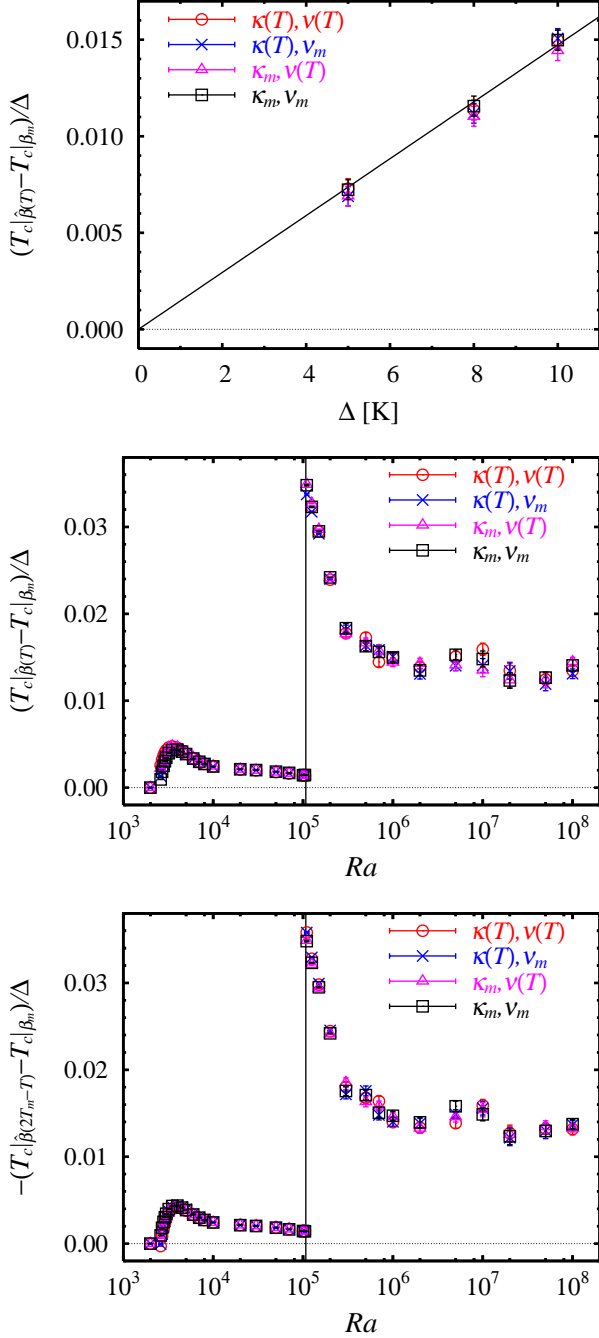
FIG. 15: Effect of the temperature dependence of the thermal expansion coefficient $\hat{\beta}$ on the shift of the center temperature for several hypothetical fluids. DNS results for the normalized temperature difference $(T_c|_{\hat{\beta}(T)} - T_c|_{\beta_m})/\Delta$ (or $-(T_c|_{\hat{\beta}(2T_m-T)} - T_c|_{\beta_m})/\Delta$) with the same temperature dependence of the thermal diffusivity κ and the kinematic viscosity ν are plotted; here $T_c|_{\hat{\beta}(T)}$ denotes the center temperature with the full temperature dependence of the buoyancy $g(1 - \rho/\rho_m)$ as given in Table I, and $T_c|_{\beta_m}$ denotes that with the linear temperature dependence $g(1 - \rho(T)/\rho_m) = C_1(T - T_m)$ only. The top panel shows $(T_c|_{\hat{\beta}(T)} - T_c|_{\beta_m})/\Delta$ versus Δ at fixed Rayleigh number $Ra = 10^6$. The solid line shows the linear fit $1.473 \cdot 10^{-3} \mathrm{K}^{-1} \times \Delta$ for the case $\hat{\beta}(T), \kappa_m, \nu_m$ (see Table II). The middle panel shows $(T_c|_{\hat{\beta}(T)} - T_c|_{\beta_m})/\Delta$ versus Ra at fixed temperature difference $\Delta = 10\mathrm{K}$. The bottom panel has the same parameters as the middle one, except showing $-(T_c|_{\hat{\beta}(2T_m-T)} - T_c|_{\beta_m})/\Delta$ for the case of mirror transformed $\hat{\beta}$.

in cylindrical cells of aspect ratio $\Gamma = 0.5$ and 1, reaching Ra numbers $O(10^{10})$. The experimental measurements at $T_m = 27°\mathrm{C}$, $P/P_* = 1.062$ (and $\Gamma = 1$) have been chosen for comparison with those at $T_m = 40°\mathrm{C}$. Contrary to the good agreement observed for the case of gas-like ethane [43], the BL theory here gives much smaller values of the center temperature shift as experiment.

Third, direct numerical simulations DNS, based on T-dependent material parameters but still within the incompressible approximation and a two-dimensional domain have been performed to get more insight into the observed discrepancy between experiment and extended BL theory. The DNS results provide a satisfactory agreement with experiment both in the gas-like as well as in the liquid-like cases. Several hypothetical ethane-like fluids have been investigated too. Our analysis shows that the extended BL predictions fail whenever the non-linear temperature dependence of the density $\rho(T)$ is implemented in the numerical simulations. Furthermore, if the dependence of $\hat{\beta}(T)$ on T dominates the NOB effects, the sign of the linear term in the effective expansion function $\hat{\beta}(T)$ is responsible for the sign of the variations of T_c as compared to the OB value $T_c = T_m$. But even if the difference $\hat{\beta}(T) - \beta_m$ is a non linear function of the temperature, the tiny T_c shift detected in our simulations is proportional to $T_c|_{\hat{\beta}(T)} - T_c|_{\beta_m}$.

Our results can be summarized in the following physical picture of the surprising phenomenon that the center temperature T_c in liquid-like ethane near its critical point increases, the center becomes warmer than the arithmeric mean temperature T_m, while in gas-like ethane the center gets colder, T_c is less than T_m. Namely, in the liquid-like case the buoyancy $\propto (T - T_m)\hat{\beta}(T)$ is larger at the bottom and smaller at the top, supporting the uprising warmer plumes more than the down coming colder top plumes. This brings predominantly hotter material into the bulk. For gas-like ethane the buoyancy is larger at the cooler top, which accelerates the downgoing cold plumes with more preference than the uprising warm plumes from the bottom, that experience a weaker buoyancy. This in turn brings more cooler material into the bulk, leading to $T_c < T_m$. It is the sign of the slope of $\hat{\beta}$ (or of β), which is the relevant quantity.

The more general lesson which can be drawn from this paper is that there is a plethora of origins of NOB corrections. Which one dominates can only be said by having a detailed look at the temperature dependence of all material parameters. Both the extended BL theory and 2D DNS are useful tools to judge which temperature dependence is the most relevant one or whether they all matter, as we now have often seen.

APPENDIX A: BOUNDARY-LAYER EQUATIONS

1. Viscous boundary-layer

Consider two-dimensional flow over a flat plate, such that the main wind velocity U does not depend on x and $\lim_{z \to \infty} u_x(x, z) = U$. Then, the x-momentum near the wall is governed by [50]

$$\rho \left\{ u_x \frac{\partial u_x}{\partial x} + u_z \frac{\partial u_x}{\partial z} \right\} = \eta \left\{ \frac{\partial^2 u_x}{\partial x^2} + \frac{\partial^2 u_x}{\partial z^2} \right\} \qquad \text{(A1)}$$
$$+ \frac{\partial \eta}{\partial z} \left\{ \frac{\partial u_x}{\partial z} + \frac{\partial u_z}{\partial x} \right\}$$
$$+ \frac{\partial}{\partial x} \left\{ \left[\frac{\eta}{3} + \zeta \right] \left[\frac{\partial u_x}{\partial x} + \frac{\partial u_z}{\partial z} \right] \right\},$$

where η is the dynamic shear viscosity and ζ the volume expansion viscosity.

To appraise the dominant structure of equation (A1) at sufficiently large Reynolds numbers, we follow Prandtl's scaling:

$$x = L \, \tilde{x}, \qquad \text{(A2)}$$
$$z = \frac{L}{\sqrt{\text{Re}}} \, \tilde{z}, \qquad \text{(A3)}$$
$$u_x = U \, \tilde{u}_x, \qquad \text{(A4)}$$
$$u_z = \frac{U}{\sqrt{\text{Re}}} \, \tilde{u}_z, \qquad \text{(A5)}$$

where L denotes the typical length of the plate in flow direction and $\text{Re} = L \, U \, \rho_m / \eta_m$ the Reynolds number. The index m indicates that the fluid properties are evaluated at a thermodynamic reference state (T_m, P_m, ρ_m), which is adopted in the nondimensionalization of $\rho \equiv \rho_m \, \tilde{\rho}$ and $\eta \equiv \eta_m \tilde{\eta}$. Then, substituting (A2)-(A5) into (A1), one finds

$$\tilde{\rho} \left\{ \tilde{u}_x \frac{\partial \tilde{u}_x}{\partial \tilde{x}} + \tilde{u}_z \frac{\partial \tilde{u}_x}{\partial \tilde{z}} \right\} = \tilde{\eta} \left\{ \frac{1}{\text{Re}} \frac{\partial^2 \tilde{u}_x}{\partial \tilde{x}^2} + \frac{\partial^2 \tilde{u}_x}{\partial \tilde{z}^2} \right\} \quad \text{(A6)}$$
$$+ \frac{\partial \tilde{\eta}}{\partial \tilde{z}} \left\{ \frac{\partial \tilde{u}_x}{\partial \tilde{z}} + \frac{1}{\text{Re}} \frac{\partial \tilde{u}_z}{\partial \tilde{x}} \right\}$$
$$+ \frac{1}{\text{Re}} \frac{\partial}{\partial \tilde{x}} \left\{ \tilde{\eta}_0 \left[\frac{\partial \tilde{u}_x}{\partial \tilde{x}} + \frac{\partial \tilde{u}_z}{\partial \tilde{z}} \right] \right\},$$

where $\tilde{\eta}_0 = \tilde{\eta} \left[\frac{1}{3} + \frac{\zeta}{\eta} \right]$. Clearly, all terms on the left-hand side of equation (A6) are of order unity. However, this is not the case on the right-hand side of (A6): only the viscous contributions involving *transverse* gradients of u_x

are of order 1; the remaining terms are of order $1/\text{Re}$.[‡]

Therefore, at large Re, the dominant part of the x-momentum equation is given by

$$\tilde{\rho} \left\{ \tilde{u}_x \frac{\partial \tilde{u}_x}{\partial \tilde{x}} + \tilde{u}_z \frac{\partial \tilde{u}_x}{\partial \tilde{z}} \right\} = \tilde{\eta} \frac{\partial^2 \tilde{u}_x}{\partial \tilde{z}^2} + \frac{\partial \tilde{\eta}}{\partial \tilde{z}} \frac{\partial \tilde{u}_x}{\partial \tilde{z}}.$$

2. Thermal boundary-layer

Consider again two-dimensional, subsonic, and steady flow over a flat plate. In the framework of boundary-layer theory, energy conservation leads to the following equation for the entropy per mass s [41]:

$$u_x \, \rho \, T \frac{\partial s}{\partial x} + u_z \, \rho \, T \frac{\partial s}{\partial z} = \frac{\partial}{\partial z} \left\{ \Lambda \frac{\partial T}{\partial z} \right\}. \qquad \text{(A7)}$$

Letting $s = s(T, \rho)$, the entropy gradient (say, its $\partial_z s$ component) can be expressed as

$$\frac{\partial s}{\partial z} = \left(\frac{\partial s}{\partial T} \right)_\rho \frac{\partial T}{\partial z} + \left(\frac{\partial s}{\partial \rho} \right)_T \frac{\partial \rho}{\partial z}.$$

The first contribution is directly associated with the isochoric specific heat (per mass) of the gas

$$T \left(\frac{\partial s}{\partial T} \right)_\rho \equiv c_V \equiv \frac{c_P}{\gamma}.$$

The second contribution follows from a Maxwell relation,

$$\left(\frac{\partial s}{\partial \rho} \right)_T = -\frac{1}{\rho^2} \left(\frac{\partial P}{\partial T} \right)_\rho = -\frac{1}{\rho \, T} \frac{c_P}{\gamma} \frac{\gamma - 1}{\beta}.$$

Thus, the left-hand side of equation (A7) can be written as

$$u_x \, \rho \, T \frac{\partial s}{\partial x} + u_z \, \rho \, T \frac{\partial s}{\partial z} = \frac{\rho \, c_P}{\gamma} \left\{ u_x \frac{\partial T}{\partial x} + u_z \frac{\partial T}{\partial z} \right\}$$
$$- \frac{c_P}{\gamma} \frac{\gamma - 1}{\beta} \left\{ u_x \frac{\partial \rho}{\partial x} + u_z \frac{\partial \rho}{\partial z} \right\}.$$

Finally, using the continuity equation $u_x \, \partial_x \rho + u_z \, \partial_z \rho = -\rho \left\{ \partial_x u_x + \partial_z u_z \right\}$, one finds

$$u_x \frac{\partial T}{\partial x} + u_z \frac{\partial T}{\partial z} + \frac{\gamma - 1}{\beta} \left\{ \frac{\partial u_x}{\partial x} + \frac{\partial u_z}{\partial z} \right\} = \frac{\gamma}{\rho \, c_P} \frac{\partial}{\partial z} \left\{ \Lambda \frac{\partial T}{\partial z} \right\}.$$

Note that the limiting case of liquids (namely $\gamma = 1$) is fully accounted by this equation.

[‡] Note that the term involving $\tilde{\nabla} \cdot \tilde{\mathbf{u}} = \frac{\partial \tilde{u}_x}{\partial \tilde{x}} + \frac{\partial \tilde{u}_z}{\partial \tilde{z}}$ is of order $1/\text{Re}$, as long as ζ and η are of the same order of magnitude. Indeed, ζ / η is of order unity if acoustical effects ($\text{Ma} \ll 1$) and chemical reactions do not take place in the fluid. For situations in which $\zeta > \eta$, see [41, Section 81].

APPENDIX B: SELF-SIMILARITY ANSATZ

1. Viscous boundary-layer

In the stream-function representation (8), the longitudinal velocity u_x is expressed as

$$u_x = \frac{1}{\tilde{\rho}}\frac{\partial}{\partial z}\{\ell_c U_c \tilde{\Psi}\} = U_c \frac{\tilde{\Psi}'}{\tilde{\rho}}$$

and its spatial derivatives are

$$\frac{\partial u_x}{\partial x} = -\frac{\nu_m}{2\ell_c^2}\frac{\tilde{Z}}{\tilde{\rho}^2}\left\{\tilde{\rho}\,\tilde{\Psi}'' - \tilde{\rho}'\,\tilde{\Psi}'\right\}, \quad (B1)$$

$$\frac{\partial u_x}{\partial z} = \frac{U_c}{\ell_c}\frac{1}{\tilde{\rho}^2}\left\{\tilde{\rho}\,\tilde{\Psi}'' - \tilde{\rho}'\,\tilde{\Psi}'\right\}, \quad (B2)$$

$$\frac{\partial^2 u_x}{\partial z^2} = \frac{U_c}{\ell_c^2}\frac{1}{\tilde{\rho}^3}\left\{\tilde{\rho}^2\,\tilde{\Psi}''' - 2\tilde{\rho}\,\tilde{\rho}'\,\tilde{\Psi}'' \right.$$
$$\left. + \left[2(\tilde{\rho}')^2 - \tilde{\rho}\,\tilde{\rho}''\right]\tilde{\Psi}'\right\}. \quad (B3)$$

Likewise, from equation (9), the transverse velocity u_z reads

$$u_z = -\frac{1}{\tilde{\rho}}\frac{\partial}{\partial x}\{U_c\,\ell_c\,\tilde{\Psi}\} = \frac{\nu_m}{2\ell_c}\left\{\tilde{Z}\frac{\tilde{\Psi}'}{\tilde{\rho}} - \frac{\tilde{\Psi}}{\tilde{\rho}}\right\},$$

with

$$\frac{\partial u_z}{\partial z} = \frac{\nu_m}{2\ell_c^2}\frac{1}{\tilde{\rho}^2}\left\{\tilde{Z}\,\tilde{\rho}\,\tilde{\Psi}'' - \tilde{Z}\,\tilde{\rho}'\,\tilde{\Psi}' + \tilde{\rho}'\,\tilde{\Psi}\right\}. \quad (B4)$$

Thus, the advective contributions in Prandtl's equation (5) can be written as

$$\rho\left\{u_x\frac{\partial u_x}{\partial x} + u_z\frac{\partial u_x}{\partial z}\right\} = -\frac{1}{2}\frac{\eta_m U_c}{\tilde{\rho}\,\ell_c^2}\left\{\tilde{\Psi}\,\tilde{\Psi}'' \right.$$
$$\left. - \frac{\tilde{\rho}'}{\tilde{\rho}}\,\tilde{\Psi}\,\tilde{\Psi}'\right\}. \quad (B5)$$

Now consider the viscous contributions:

$$\frac{\partial}{\partial z}\left\{\eta\frac{\partial u_x}{\partial z}\right\} = \eta\frac{\partial^2 u_x}{\partial z^2} + \frac{\partial\eta}{\partial z}\frac{\partial u_x}{\partial z}. \quad (B6)$$

Since

$$\frac{\partial\eta}{\partial z} = \frac{\eta_m}{\ell_c}\left\{\left(\frac{\partial\tilde{\eta}}{\partial\tilde{\Theta}}\right)_{\tilde{\rho}}\tilde{\Theta}' + \left(\frac{\partial\tilde{\eta}}{\partial\tilde{\rho}}\right)_{\tilde{\Theta}}\tilde{\rho}'\right\}, \quad (B7)$$

insertion of (B2) and (B3) into (B6) leads to

$$\frac{\tilde{\rho}\,\ell_c^2}{\eta_m U_c}\frac{\partial}{\partial z}\left\{\eta\frac{\partial u_x}{\partial z}\right\} = \tilde{\eta}\,\tilde{\Psi}''' + \left[\tilde{\eta}' - 2\frac{\tilde{\rho}'}{\tilde{\rho}}\,\tilde{\eta}\right]\tilde{\Psi}''$$
$$+ \left\{\left[2\left(\frac{\tilde{\rho}'}{\tilde{\rho}}\right)^2 - \frac{\tilde{\rho}''}{\tilde{\rho}}\right]\tilde{\eta}\right.$$
$$\left. - \frac{\tilde{\rho}'}{\tilde{\rho}}\,\tilde{\eta}'\right\}\tilde{\Psi}'. \quad (B8)$$

Therefore, by substituting (B5) and (B8) into (5) one finally obtains equation (11).

2. Thermal boundary-layer

In the same spirit as above, inserting (B1), (B4), and

$$\frac{\partial}{\partial z}\left\{\Lambda\frac{\partial T}{\partial z}\right\} = \frac{\Lambda_m\Delta}{\ell_c^2}\left\{\tilde{\Lambda}\,\tilde{\Theta}'' + \tilde{\Lambda}'\,\tilde{\Theta}'\right\}$$

into equation (6) one finds

$$-\frac{\nu_m\Delta}{2\ell_c^2}\frac{\tilde{\Psi}}{\tilde{\rho}}\tilde{\Theta}' + \frac{\nu_m}{2\ell_c^2}\frac{\gamma-1}{\beta}\frac{\tilde{\rho}'}{\tilde{\rho}^2}\tilde{\Psi} = \frac{\gamma}{\tilde{\rho}\,\tilde{c}_P}\frac{1}{\mathrm{Pr}}\left\{\tilde{\Lambda}\,\tilde{\Theta}'' + \tilde{\Lambda}'\,\tilde{\Theta}'\right\},$$

where $\tilde{\beta} = \beta\,\Delta$ and $\mathrm{Pr} = (\nu_m\,\rho_m\,c_{P,m})/\Lambda_m$. Thus

$$\tilde{\Lambda}\,\tilde{\Theta}'' + \left\{\frac{1}{2}\frac{\tilde{c}_P}{\gamma}\,\mathrm{Pr}\,\tilde{\Psi} + \tilde{\Lambda}'\right\}\tilde{\Theta}' - \frac{\gamma-1}{2\gamma}\frac{\tilde{c}_P}{\tilde{\beta}}\frac{\tilde{\rho}'}{\tilde{\rho}}\,\mathrm{Pr}\,\tilde{\Psi} = 0.$$

Here, substituting $\tilde{\rho}'$ by (12) one finally obtains

$$\tilde{\Lambda}\,\tilde{\Theta}'' + \left\{\frac{1}{2}\tilde{c}_P\,\mathrm{Pr}\,\tilde{\Psi} + \tilde{\Lambda}'\right\}\tilde{\Theta}' = 0.$$

Note that the limiting case of liquids (namely $\gamma = 1$) is fully accounted by this equation.

APPENDIX C: NUMERICAL RESULTS ON NUSSELT NUMBERS IN REAL AND HYPOTHETICAL ETHANE FLUIDS

For completeness, in table III the NOB corrections in the Nusselt number are given, resulting from the numerical simulations of real and hypothetical ethane. The corresponding NOB corrections of the center temperature had already been shown in table II.

[1] B. Castaing, G. Gunaratne, F. Heslot, L. Kadanoff, A. Libchaber, S. Thomae, X. Z. Wu, S. Zaleski, and G. Zanetti, J. Fluid Mech. **204**, 1 (1989).
[2] E. D. Siggia, Annu. Rev. Fluid Mech. **26**, 137 (1994).
[3] S. Cioni, S. Ciliberto, and J. Sommeria, J. Fluid Mech. **335**, 111 (1997).
[4] X. Chavanne, F. Chilla, B. Castaing, B. Hebral, B. Chabaud, and J. Chaussy, Phys. Rev. Lett. **79**, 3648 (1997).
[5] X. Xu, K. M. S. Bajaj, and G. Ahlers, Phys. Rev. Lett. **84**, 4357 (2000).
[6] J. Niemela, L. Skrebek, K. R. Sreenivasan, and R. Don-

case	$\hat{\beta}$	κ	ν	$100(Nu/Nu_{OB}-1)$ at $Ra=10^6$	$100(Nu/Nu_{OB}-1)$ at $Ra=10^7$	$100(Nu/Nu_{OB}-1)$ at $Ra=10^8$
1 (NOB)	$\hat{\beta}(T)$	$\kappa(T)$	$\nu(T)$	0.7097 ± 0.1517	0.8956 ± 0.2213	1.2403 ± 0.2316
2	$\hat{\beta}(T)$	$\kappa(T)$	ν_m	0.1655 ± 0.1511	0.4795 ± 0.2323	0.4040 ± 0.2328
3	$\hat{\beta}(T)$	κ_m	$\nu(T)$	1.3160 ± 0.1518	1.5812 ± 0.2230	1.6502 ± 0.2234
4	$\hat{\beta}(T)$	κ_m	ν_m	0.6640 ± 0.1505	0.4963 ± 0.2324	0.6450 ± 0.2425
5	$\hat{\beta}(2T_m - T)$	$\kappa(T)$	$\nu(T)$	1.0087 ± 0.1518	1.2804 ± 0.2214	1.3223 ± 0.2228
6	$\hat{\beta}(2T_m - T)$	$\kappa(T)$	ν_m	0.1655 ± 0.1511	0.4795 ± 0.2323	0.4040 ± 0.2328
7	$\hat{\beta}(2T_m - T)$	κ_m	$\nu(T)$	0.9925 ± 0.1518	1.1741 ± 0.2255	1.0832 ± 0.2329
8	$\hat{\beta}(2T_m - T)$	κ_m	ν_m	0.5988 ± 0.1505	0.9991 ± 0.2236	1.0073 ± 0.2286
9	β_m	$\kappa(T)$	$\nu(T)$	0.3425 ± 0.1517	0.6188 ± 0.2175	0.0538 ± 0.2455
10	β_m	$\kappa(T)$	ν_m	-0.1734 ± 0.1509	-0.4404 ± 0.2277	0.0195 ± 0.2246
11	β_m	κ_m	$\nu(T)$	0.6380 ± 0.1523	0.4491 ± 0.2321	0.7775 ± 0.2222
12 (OB)	β_m	κ_m	ν_m	0.0000 ± 0.1070	0.0000 ± 0.1573	0.0000 ± 0.1689

TABLE III: Simulation results of the relative deviation of the Nusselt number $Nu/Nu_{OB} - 1$ at the temperature difference of $\Delta = 10K$ for several hypothetical fluids. At the Rayleigh numbers of $Ra = 10^6$, 10^7, and 10^8 the OB Nusselt numbers correspond to $Nu_{OB} = 6.53$, 12.43, and 25.12, respectively. The notations for the material properties are the same as in Table II.

nelly, Nature **404**, 837 (2000).

[7] X. Chavanne, F. Chilla, B. Chabaud, B. Castaing, and B. Hebral, Phys. Fluids **13**, 1300 (2001).

[8] G. Ahlers and X. Xu, Phys. Rev. Lett. **86**, 3320 (2001).

[9] X. L. Qiu and P. Tong, Phys. Rev. E **64**, 036304 (2001).

[10] L. P. Kadanoff, Phys. Today **54**, 34 (2001).

[11] K.-Q. Xia, S. Lam, and S. Q. Zhou, Phys. Rev. Lett. **88**, 064501 (2002).

[12] P. E. Roche, B. Castaing, B. Chabaud, and B. Hebral, Europhys. Lett. **58**, 693 (2002).

[13] J. Niemela and K. R. Sreenivasan, J. Fluid Mech. **481**, 355 (2003).

[14] D. Funfschilling and G. Ahlers, Phys. Rev. Lett. **92**, 194502 (2004).

[15] E. Brown, D. Funfschilling, and G. Ahlers, Phys. Rev. Lett. **95**, 084503 (2005).

[16] A. Nikolaenko, E. Brown, D. Funfschilling, and G. Ahlers, J. Fluid Mech. **523**, 251 (2005).

[17] J. Niemela and K. R. Sreenivasan, J. Fluid Mech. **557**, 411 (2006).

[18] K.-Q. Xia, C. Sun, and S. Q. Zhou, Phys. Rev. E **68**, 066303 (2003).

[19] X. D. Shang, X. L. Qiu, P. Tong, and K.-Q. Xia, Phys. Rev. Lett. **90**, 074501 (2003).

[20] P. E. Roche, B. Castaing, B. Chabaud, and B. Hebral, J. Low. Temp. Phys. **134**, 1011 (2004).

[21] C. Sun, K. Q. Xia, and P. Tong, Phys. Rev. E **72**, 026302 (2005).

[22] E. Brown and G. Ahlers, J. Fluid Mech. **568**, 351 (2006).

[23] J. Niemela and K. R. Sreenivasan, J. Low. Temp. Phys. **143**, 163 (2006).

[24] R. du Puits, C. Resagk, A. Tilgner, F. H. Busse, and A. Thess, J. Fluid Mech. **572**, 231 (2007).

[25] R. Kerr, J. Fluid Mech. **310**, 139 (1996).

[26] R. Benzi, F. Toschi, and R. Tripiccione, J. Stat. Phys. **93**, 901 (1998).

[27] R. Kerr and J. R. Herring, J. Fluid Mech. **419**, 325 (2000).

[28] R. Verzicco and R. Camussi, J. Fluid Mech. **383**, 55

(1999).

[29] R. Verzicco and R. Camussi, J. Fluid Mech. **477**, 19 (2003).

[30] D. Lohse and F. Toschi, Phys. Rev. Lett. **90**, 034502 (2003).

[31] R. Verzicco, Phys. Fluids **16**, 1965 (2004).

[32] G. Amati, K. Koal, F. Massaioli, K. R. Sreenivasan, and R. Verzicco, Phys. Fluids **17**, 121701 (2005).

[33] O. Shishkina and C. Wagner, J. Fluid Mech. **546**, 51 (19).

[34] G. Stringano and R. Verzicco, J. Fluid Mech. **548**, 1 (2006).

[35] R. P. J. Kunnen, H. J. H. Clercx, B. J. Geurts, L. A. Bokhoven, R. A. D. Akkermans, and R. Verzicco, Phys. Rev. E **77**, 016302 (2008).

[36] S. Grossmann and D. Lohse, J. Fluid Mech. **407**, 27 (2000). Phys. Rev. Lett. **86**, 3316 (2001). Phys. Rev. E **66**, 016305 (2002). Phys. Fluids **16**, 4462 (2004).

[37] R. Benzi, Phys. Rev. Lett. **95**, 024502 (2005).

[38] E. Brown and G. Ahlers, Phys. Rev. Lett. **98**, 134501 (2007).

[39] A. Oberbeck, Ann. Phys. Chem. **7**, 271 (1879).

[40] J. Boussinesq, *Theorie analytique de la chaleur, Vol. 2* (Gauthier-Villars, Paris, 1903).

[41] L. D. Landau and E. M. Lifshitz, *Fluid Mechanics* (Pergamon Press, Oxford, 1987).

[42] S. Chandrasekhar, *Hydrodynamic and Hydromagnetic Stability* (Dover, New York, 1981).

[43] G. Ahlers, E. Brown, F. Fontenele Araujo, D. Funfschilling, S. Grossmann, and D. Lohse, J. Fluid Mech. **569**, 409 (2006).

[44] J. Zhang, S. Childress, and A. Libchaber, Phys. Fluids **9**, 1034 (1997).

[45] K. Sugiyama, E. Calzavarini, S. Grossmann, and D. Lohse, Europhys. Lett. **80**, 34002 (2007).

[46] G. Ahlers, F. Fontenele Araujo, D. Funfschilling, S. Grossmann, and D. Lohse, Phys. Rev. Lett. **98**, 054501 (2007).

[47] D. G. Friend, H. Ingham, and J. F. Ely, J. Phys. Chem.

Ref. Data **20**, 275 (1991).

[48] S. Ciliberto, S. Cioni, and C. Laroche, Phys. Rev. E **54**, R5901 (1996).

[49] G. Ahlers, E. Brown, and A. Nikolaenko, J. Fluid Mech. **557**, 347 (2006).

[50] H. Schlichting and K. Gersten, *Boundary layer theory* (Springer Verlag, Berlin, 2000), 8th ed.

[51] K. Stewartson, *The theory of laminar boundary layers in compressible fluids* (Oxford University Press, 1964).

[52] R. Krishnamurti and L. N. Howard, Proc. Natl. Acad. Sci. **78**, 1981 (1981).

[53] W. Press, S. Teukolsky, W. Vetterling, and B. Flannery, *Numerical Recipes* (Cambridge University Press, Cambridge, 1986).

[54] G. Ahlers, D. S. Cannell, L. I. Berge, and S. Sakurai, *Phys. Rev. E* **49**, 545-553 (1994).

[55] K. Müller, G. Ahlers, and F. Pobell, Phys. Rev. B **14**, 2096 (1976).

[56] G. Ahlers, Phys. Rev. E **63**, 015303 (2000).

[57] P. Roche, B. Castaing, B. Chabaud, B. Hebral, and J. Sommeria, Eur. Phys. J. B **24**, 405 (2001).

[58] E. Brown, D. Funfschilling, A. Nikolaenko, and G. Ahlers, Phys. Fluids **17**, 075108 (2005).

[59] E. Brown and G. Ahlers, EPL **80**, 14001 (2007).

[60] K. Sugiyama, E. Calzavarini, S. Grossmann, and D. Lohse, J. Fluid Mech., to be submitted (2008).